

Seismic wave modeling of fluid-saturated fractured porous rock: Including fluid pressure diffusion effects of discrete distributed large-scale fractures

Yingkai Qi^{1,2}, Xuehua Chen^{1,2}, Qingwei Zhao^{1,2}, Xin Luo¹, Chunqiang Feng³

¹State Key Laboratory of Oil & Gas Reservoir Geology and Exploitation, Chengdu University of Technology, Chengdu, 610059, China

²Key Laboratory of Earth Exploration & Information Techniques of Ministry of Education, Chengdu University of Technology, Chengdu, 610059, China

³Exploration & Development Research Institute of Henan Oilfield, Sinopec, 473000, China

Correspondence to: Xuehua Chen (chen_xuehua@163.com)

Abstract. The scattered seismic waves of fractured porous rock are strongly affected by the wave-induced fluid pressure diffusion effects between the compliant fractures and the stiffer embedding background. To include these poroelastic effects in seismic modeling, we develop a numerical scheme for discrete distributed large-scale fractures embedded in fluid-saturated porous rock. Using Coates and Schoenberg's local effective medium theory and Barbosa's dynamic linear slip model characterized by complex-valued and frequency-dependent fracture compliances, we derive the effective viscoelastic compliances in each spatial discretized cell by superimposing the compliances of the background and the fractures. The effective governing equations for fractured porous rocks are viscoelastic anisotropic and numerically solved by mixed-grid stencil frequency-domain finite-difference method. The main advantage of our proposed modeling scheme over poroelastic modeling schemes is that the fractured domain can be modeled using a viscoelastic solid, while the rest of the domain can be modeled using an elastic solid. We have tested the modeling scheme in a single fracture model, a fractured model, and a modified Marmousi model. The good consistency between the scattered waves off a single horizontal fracture calculated using our proposed scheme and the poroelastic modeling validates that our modeling scheme can properly capture the FPD effects. In the case of a set of aligned fractures, the scattered waves from the top and bottom of the fractured reservoir are strongly influenced by the FPD effects, and the reflected waves from the underlying formation can retain the relevant attenuation and dispersion information. The proposed numerical modeling scheme can also be used to improve migration quality and the estimation of fracture mechanical characteristics in inversion.

1 Introduction

Fluid saturated porous rocks in a reservoir, which are characterized by a heterogeneous internal structure consisting of a solid skeleton and interconnected fluid-filled voids, are often permeated by much more compliant and permeable fractures. Although the fractures typically occupy only a small volume, they tend to dominate the overall mechanical and hydraulic properties of

31 the reservoir (Liu et al., 2000; Gale et al., 2014). Thus, fracture detection, characterization, and imaging are of great importance
32 for hydrocarbon exploration and production. Seismic waves are widely used for these purposes because their amplitude, phase,
33 and anisotropy properties can be strongly affected by the fractures (Chapman, 2003; Gurevich, 2003; Brajanovski et al., 2005;
34 Carcione et al., 2011; Rubino et al., 2014). Therefore, appropriate numerical modeling methods are required for the
35 interpretation, migration and inversion of seismic data from porous media containing discrete distributed fractures.

36 Biot's poroelastic theory (Biot, 1956a; b) is the fundamental theory to describe elastic wave propagation in fluid porous media,
37 including the dynamic interactions between rock and pore fluid. However, the original theory, assuming a macroscopically
38 homogeneous porous media saturated by a single fluid phase, fails to explain the measured velocity dispersion and attenuation
39 of seismic waves (Nakagawa et al., 2007). In recent decades, many researchers have found that if porous media contains
40 mesoscale heterogeneity, a local fluid-pressure gradient will be induced at a scale comparable to the fluid pressure diffusion
41 length at the seismic frequency band, thus causing significant velocity dispersion and attenuation (White et al., 1975; Dutta
42 and Odé, 1979; Johnson, 2001; and Müller et al. 2008; Norris, 1993; Gurevich et al., 1997; Gelinsky and Shapiro, 1997;
43 Kudarova et al., 2016). Fractures embedded in homogeneous porous background are special heterogeneities, exhibiting strong
44 mechanical contrasts with background. When seismic waves travel through fluid saturated fractured porous rocks, local fluid
45 pressure gradients will be induced between the fractures and the background in response to the strong compressibility contrast.
46 To return the equilibrium state, fluid pressure diffusion (FPD) occurs between the fractures and the embedding background,
47 which in turn changes the fluid stiffening effect on the fractures and thus their mechanical compliances depending on frequency
48 (Barbosa et al., 2016a, b).

49 When the fractures with spacing and length much smaller than the wavelengths are uniformly and regularly distributed, the
50 properties of the fractured rocks are homogeneous at macroscopic scale and can be described by a representative elementary
51 volume (REV). Various effective medium theories are available for estimating the fracture-induced anisotropy, attenuation,
52 and dispersion in a poroelastic context (Hudson, 1981; Thomsen, 1995; Chapman, 2003; Brajanovski et al., 2005; Krzikalla et
53 al. 2011; Galvin et al., 2015; Guo et al., 2017a; b). However, large-scale fractures with much larger spacing and length typically
54 have a more complex discrete distribution rather than a regular one, therefore the properties of rocks containing such fractures
55 cannot be modeled by the effective medium theory. In contrast, the linear slip model (LSM) (Schoenberg, 1980), which
56 represents individual fractures as nonwelded interfaces with discontinuous displacement tensors, is not limited by the
57 assumption of regular distribution and can be used to model the discretely distributed fractures. Due to the discrete distribution,
58 the effects of large-scale fractures are not uniform and vary spatially, which mean that their effects cannot be represented by a
59 single REV. In the framework of LSM, two numerical schemes are available to assess the seismic response of discrete
60 distributed large-scale fractures, the local effective-medium schemes (Coates and Schoenberg, 1995; Igel et al., 1997; Vlastos
61 et al., 2003; Oelke, et al., 2013) and the explicit interface scheme (Zhang, 2005; Cui et al., 2018; Khokhlov, et al., 2021). The
62 local effective-medium scheme uses a very coarse mesh to discretize background media and incorporates the additional effects

63 of fractures within each discretized cell based on LSM, that is, it regards each discretized cell as a REV. The advantage is that
64 it requires no special treatment of the displacement discontinuity conditions on the fractures, which means no additional
65 memory and computation costs. The explicit interface scheme uses a very fine mesh to discretize fractures and directly treats
66 the displacement discontinuity across each fracture without any equivalent treatment, resulting in expensive memory and
67 computation costs.

68 The common aspect of the aforementioned numerical modeling schemes is that they are all implemented in a purely elastic
69 LSM with real-valued compliances boundary and represent both the embedding background and fractures as elastic solids, thus
70 the impact of FPD effects on seismic scattering can't be accounted for. A dynamic linear slip model incorporating FPD effects
71 should be considered when implementing numerical modeling of seismic wave propagating in fluid saturated porous rocks
72 containing discrete distributed large-scale fractures. Nakagawa and Schoenberg (2007) developed an extended poroelastic
73 LSM (PLSM) for a single fracture. The proposed model representing both the background and the fracture as poroelastic media
74 can appropriately incorporate the frequency related effects, but it will also result in a higher computational consuming and
75 more memory requirements. Rubino et al. (2015) proposed a frequency-dependent complex-valued normal compliance for a
76 set of aligned fractures with a separation much smaller than the prevailing seismic wavelength. Despite the ability of including
77 the FPD across the fractures, the model is not suitable for modeling discrete distributed fractures. In the context of
78 viscoelasticity, Barbosa et al. (2016a) developed a viscoelastic linear slip model (VLSM) for an individual fracture with explicit
79 complex-valued and frequency-dependent fracture compliances, to account for the impact of FPD on the fracture stiffness.
80 That provides a viscoelasticity-based modeling algorithm for discrete distributed large-scale fractures with smaller
81 computational costs and memory requirements than the poroelasticity based modeling.

82 In this paper, we develop a viscoelastic numerical modeling scheme to simulate seismic wave propagation in fluid-saturated
83 porous media containing discrete distributed large-scale fractures. To capture the FPD effects between the fractures and
84 background, we use the local effective medium theory based on Barbosa's VLSM to derive the effective anisotropic
85 viscoelastic compliances in each numerical cell by superimposing the compliances of the background and the fractures. The
86 effective anisotropic viscoelastic governing equations of the fractured porous rock are then numerically solved using mixed-
87 grid stencil frequency-domain finite-difference method (FDFD) (Hustedt, et al. 2004; Operto, et al. 2009; Liu et al., 2018).
88 Compare to poroelastic modeling scheme, the main advantage of our modeling scheme is that it uses VLSM-based viscoelastic
89 modeling to account for FDP effects in the domain permeated by fractures, while in the rest fracture-free domain, it uses elastic
90 modeling. To validate the proposed viscoelastic modeling scheme can capture the impact of FPD effects on seismic wave
91 scattering, we compare the scattered waves of a single horizontal fracture obtained using our proposed modeling scheme with
92 poroelastic modeling scheme and elastic modeling scheme. Numerical examples of a fractured reservoir are presented to
93 demonstrate that the proposed modeling scheme can properly simulate the wave attenuation and dispersion due to the FPD
94 effects between the fracture system and background. A set of rock physics models were generated by the Marmousi model to

test the proposed modeling scheme and code. The scheme can be used not only to study the impact of mechanical and hydraulic of fracture properties on seismic scattering but can also to improve migration quality and the estimation of fracture mechanical characteristics in inversion.

2 Review of the LSM

The LSM was originally proposed by Schoenberg (1980) to represent a solid- or fluid-infilled fracture permeated in a pure solid background, and then extended by other researchers (e.g. Nakagawa, Barbosa) to represent a poroelastic fracture to include the FPD effects. We briefly review the original LSM and its poroelastic and viscoelastic extensions.

2.1 The original LSM

Schoenberg (1980) presented the original LSM in the context of elasticity, representing both the background and the fracture as elastic solids. The original LSM assumes that across a fracture surface the stresses are continuous while the displacements are discontinuous. The discontinuous displacement vector of a horizontal fracture is linearly related to the stress tensor through the fracture compliance, which can be written as:

$$\begin{aligned} [u_x] &= Z_T \sigma_{xz}, \\ [u_y] &= Z_T \sigma_{yz}, \\ [u_z] &= Z_N \sigma_{zz}, \end{aligned} \quad (1)$$

where $[u_i]$ are the discontinuous displacement components, σ_{ij} are the stress components, $Z_N = h/H$ and $Z_T = h/\mu$ are the normal and tangential compliance of the fracture, respectively. H and μ are the P -wave and shear modulus of the fracture, and h is the thickness of the fracture. Due to the simple expression, the original LSM can be easily incorporated into the local effective medium theory to model seismic wave scattering off large-scale fractures. However, the original LSM was derived in a purely elastic context, only suitable for fractures filled with pure solids or fluids, thus it is not competent to describe the FPD effects.

2.2 Nakagawa's PLSM

Nakagawa and Schoenberg (2007) presented a PLSM in the framework of poroelasticity, representing the fracture as a highly compliant and porous thin isotropic, homogeneous layer embedded in a much stiffer and much less porous background (Nakagawa et al., 2007, Barbosa et al., 2016a). Similar to the classic LSM, the PLSM assumes that across a fracture surface the stresses are continuous while the displacements are discontinuous. The discontinuous displacement components for a horizontal fracture are (Nakagawa and Schoenberg, 2007):

$$\begin{aligned}
[u_x] &= Z_T \sigma_{xz}, \\
[u_y] &= Z_T \sigma_{yz}, \\
[u_z] &= Z_{N_D} (\sigma_{zz} + \alpha P_f), \\
[w_z] &= -\alpha Z_{N_D} \left(\sigma_{zz} + \frac{1}{B} P_f \right),
\end{aligned} \tag{2}$$

where $Z_{N_D} = h/H_D$ and $Z_T = h/\mu$ are the fracture's drained normal compliance and tangential compliance, respectively, H_D and H_U are the fracture's drained and undrained P -wave modulus, respectively, α is the Biot's effective stress coefficient of the fracture, $B = \alpha M/H_U$ is the fracture's uniaxial Skempton coefficient. Since the PLSM represents both the background and the fracture as poroelasticity, it is capable to describe the discontinuous displacement of the relative fluid in addition to the solid, implying that it can properly handle the FPD effects between the background and the fracture. Although it is difficult to incorporate the PLSM into the effective medium theory to obtain the effective moduli of the fractured porous rock, these boundary conditions can be easily incorporated into poroelastic finite-difference algorithm for modeling seismic wave scattering off large-scale fractures parallel to the coordinate axis. An alternative wavenumber domain method for modeling the scattered waves by poroelastic fractures is presented by Nakagawa and Schoenberg (2007) based on the PLSM.

2.3 Barbosa's VLSM

Barbosa et al. (2016a) derived a VLSM that account for the FPD effects between a fracture and background and the resulting stiffening effect impact on the fracture. The background is assumed to be not impacted by the FPD and can be represented by an elastic solid, whose properties are computed according to Gassmann's equation. By representing fractures as extremely thin viscoelastic layers, the poroelastic effects were incorporated into the classical LSM through complex-valued and frequency-dependent compliances. These compliances characterize the mechanical properties of the fluid-saturated fracture.

The discontinuous displacement components of the VLSM (Barbosa et al., 2016a) for a horizontal fracture are

$$\begin{aligned}
[u_x] &= Z_T \sigma_{xz}, \\
[u_y] &= Z_T \sigma_{yz}, \\
[u_z] &= Z_N \sigma_{zz} + Z_X \varepsilon_{xx},
\end{aligned} \tag{3}$$

where Z_N and Z_T are generalized normal and tangential compliances of the fracture respectively, and Z_X is a dimensionless parameter that related to the coupling between horizontal and vertical deformation of the fracture. The normal compliance Z_N and additional parameter Z_X are complex-valued and frequency-dependent, while the tangential compliance $Z_T = h/\mu$ is the same as for elastic and poroelastic models. The two frequency-dependent and complex-valued compliances are:

$$\begin{aligned}
Z_N &= Z_{N_U} + Z_{N_D} \frac{G_1(1+i)}{\sqrt{\omega} + G_2(1+i)}, \\
Z_X &= -\frac{G_3(1+i)}{\sqrt{\omega} + G_4(1+i)},
\end{aligned} \tag{4}$$

143 where $Z_{N_U} = h/H_U$ and $Z_{N_D} = h/H_D$ are the fracture's undrained and drained normal compliance respectively, ω is the angular
 144 frequency. The four real-valued parameters G_1, G_2, G_3 and G_4 are defined as

$$145 \quad G_1 = \frac{\kappa^b}{\eta Z_{N_D}} \frac{(B^b - B^f)^2}{\sqrt{D^b}}, \quad G_2 = \frac{\kappa^b}{\eta Z_{N_D}} \frac{B^f}{\alpha^f \sqrt{D^b}}, \quad G_3 = \frac{2\sqrt{2}\alpha^b \mu^b (B^f - B^b) \sqrt{D^b}}{H_D^b}, \quad G_4 = \frac{\sqrt{2}\kappa^b D^f}{Z_T \mu^f \kappa^f \sqrt{D^b}}, \quad (5)$$

146 where κ is the permeability, η is the viscosity of the fluid, $D = \frac{\kappa H_D M}{\eta H_U}$ is the diffusivity, the other parameters are defined in
 147 the same way as in poroelasticity. The parameters in equation (5) with superscripts b correspond to background properties and
 148 the parameters with superscripts c correspond to fracture parameters.

149 In the low-frequency limit, the two frequency-dependent and complex-valued parameters become:

$$150 \quad \begin{aligned} Z_N &= Z_{N_U} + Z_{N_D} \frac{G_1}{G_2}, \\ Z_X &= -\frac{G_3}{G_4}. \end{aligned} \quad (6)$$

151 The frequency-independent and real-valued parameters in equation (6) indicate the elastic behavior of the fracture, which is
 152 expected, since the fluid pressure between the fracture and background at low frequencies has enough time to equilibrate within
 153 a half-wave period (i.e. the fracture is softest), resulting in no dispersion and attenuation of the seismic waves.

154 In the high-frequency limit, the two frequency-dependent and complex-valued parameters become:

$$155 \quad \begin{aligned} Z_N &= Z_{N_U}, \\ Z_X &= 0. \end{aligned} \quad (7)$$

156 Equation (7) indicates that the fracture model collapses to an elastic thin layer model in the high-frequency limit, which is
 157 consistent with the original LSM that computes the properties of both fracture and background using Gassmann's equations.
 158 This because at high frequencies, the fluid pressure between the fracture and background has no time to equilibrate within a
 159 half-wave period, i.e. the fracture is hardest and behaves as being sealed. The VLSM considering FPD effects can be
 160 incorporated into the local effective medium theory to simulate the poroelastic seismic response of large-scale fractures, while
 161 its low- and high-frequency limits can be used to model the elastic seismic response.

162 In the VLSM, according to Barbosa et al. (2016a), there are two distinct frequency regimes frequency-dependent fracture
 163 compliance due to FPD, and the characteristic frequency for the transition between the two regimes is:

$$164 \quad \omega_m = 2\pi f_m = \left(\frac{2}{h}\right)^2 \left(\frac{e_b^2}{e_f^2 + e_f e_b}\right) D_f, \quad (8)$$

165 where h is the thickness of the fracture, D is the diffusivity, $e = \kappa/\eta\sqrt{D}$, the superscripts b and f correspond to background
 166 fracture parameters, respectively.

3 Seismic modeling of fractured porous rock

In this section, we focus on the implementation of seismic modeling of fluid-saturated porous media containing discrete distributed large-scale fractures in 2D case. We develop a viscoelastic modeling scheme based on the VLSM and local effective medium theory (Coates and Schoenberg, 1995) to incorporate the FPD effects between fractures and background. To validate that the proposed viscoelastic modeling scheme can capture the impact of FPD effects on seismic wave scattering of fractures, we outline the implementation of poroelastic modeling scheme using an explicit application of the PLSM.

3.1 viscoelastic modeling based on VLSM

To incorporate the VLSM into viscoelastic finite-difference modeling algorithms, we adopt Coates and Schoenberg's local effective media theory (1995) to account for the property of each fracture. We first provide the specific derivation of the effective viscoelastic-anisotropic stiffness matrix of the numerical cell by superimposing the compliances of the background and the fractures. The porous background is assumed to be unaffected by the FPD in the presence of fractures because of the small amount of diffusing fluid and large compliance contrast between background and fluid. Thus, the rock background can be represented by an elastic homogeneous solid and its strain tensor ϵ^b can be expressed as

$$\epsilon_{ij}^b = s_{ijkl}^b \sigma_{kl}, \quad (i, j = x, y, z) \quad (9)$$

where the compliance tensor s^b is computed according to Gassmann's equation (Rubino et al., 2015), and σ is the average stress tensor. The exceed strain tensor ϵ^c induced by a single fracture with surface S in a representative volume V (e.g. the volume of numerical cell) is given by (Hudson and Knopoff, 1989; Sayers and Kachanov, 1995; Liu, et al., 2000)

$$\epsilon_{ij}^c = s_{ijkl}^c \sigma_{kl} = \frac{1}{2V} \int ([u_i] n_j + [u_j] n_i) dS, \quad (10)$$

where s^c is the extra compliance tensor resulting from the fractures, $[u_i]$ is the i th component of the displacement discontinuity on S , n_i is the i th component of the fracture normal. Note that equation (10) is applicable to finite, nonplanar fractures in the long wavelength limit, i.e., the applied stress is assumed to be constant over the representative volume.

If we assume that the interface of the fracture is normal to the z -axis (fracture normal vector \mathbf{n} is $(0,0,1)$), substituting equation (3) into equation (10), we can obtain the nonzero element of the exceed fracture strain tensor:

$$\begin{aligned} \epsilon_{xz}^c &= \frac{S}{V} Z_T \sigma_{xz}, \\ \epsilon_{yz}^c &= \frac{S}{V} Z_T \sigma_{yz}, \\ \epsilon_{zz}^c &= \frac{S}{V} (Z_N \sigma_{zz} + Z_X \epsilon_{xx}^b). \end{aligned} \quad (11)$$

For simplicity, we use an abbreviated Voigt notation for the stresses, strains, and stiffness and compliance tensors, and rewrite the equation (9) and (11) as:

$$\hat{\epsilon}^b = \hat{\mathbf{S}}^b \hat{\sigma}, \quad (12)$$

$$\hat{\boldsymbol{\varepsilon}}^c = \frac{S}{V} (\hat{\mathbf{Z}}^I \hat{\boldsymbol{\sigma}} + \hat{\mathbf{Z}}^II \hat{\boldsymbol{\varepsilon}}) = \frac{S}{V} (\hat{\mathbf{Z}}^I + \hat{\mathbf{Z}}^II \hat{\mathbf{S}}^b) \hat{\boldsymbol{\sigma}}, \quad (13)$$

where $\hat{\boldsymbol{\varepsilon}} = [\varepsilon_{xx}, \varepsilon_{yy}, \varepsilon_{zz}, 2\varepsilon_{yz}, 2\varepsilon_{xz}, 2\varepsilon_{xy}]^T$ is the strain matrix, $\hat{\boldsymbol{\sigma}} = [\sigma_{xx}, \sigma_{yy}, \sigma_{zz}, \sigma_{yz}, \sigma_{xz}, \sigma_{xy}]^T$ is the stress matrix, and $\hat{\mathbf{S}}^b$ is the compliance matrix of background. Note that in this paper the " \wedge " symbol is used to indicate matrices to distinguish them from tensors, which is used to distinguish a tensor. The 6×6 fracture compliance matrix $\hat{\mathbf{Z}}^I$ and additional dimensionless matrix $\hat{\mathbf{Z}}^II$ according to the Voigt notation are defined as

$$\hat{\mathbf{Z}}^I = \begin{bmatrix} 0 & 0 & 0 & 0 & 0 & 0 \\ 0 & 0 & 0 & 0 & 0 & 0 \\ 0 & 0 & Z_N & 0 & 0 & 0 \\ 0 & 0 & 0 & Z_T & 0 & 0 \\ 0 & 0 & 0 & 0 & Z_T & 0 \\ 0 & 0 & 0 & 0 & 0 & 0 \end{bmatrix}, \quad \hat{\mathbf{Z}}^II = \begin{bmatrix} 0 & 0 & 0 & 0 & 0 & 0 \\ 0 & 0 & 0 & 0 & 0 & 0 \\ Z_X & 0 & 0 & 0 & 0 & 0 \\ 0 & 0 & 0 & 0 & 0 & 0 \\ 0 & 0 & 0 & 0 & 0 & 0 \\ 0 & 0 & 0 & 0 & 0 & 0 \end{bmatrix}, \quad (14)$$

The average strain in a homogeneous porous rock containing single fracture can be expressed as the sum of the strains of background and the fractures

$$\hat{\boldsymbol{\varepsilon}} = \hat{\boldsymbol{\varepsilon}}^b + \hat{\boldsymbol{\varepsilon}}^c. \quad (15)$$

Substituting equation (12) and (13) into equation (15), we can obtain the average strain matrix

$$\hat{\boldsymbol{\varepsilon}} = \left[\hat{\mathbf{S}}^b + \frac{S}{V} (\hat{\mathbf{Z}}^I + \hat{\mathbf{Z}}^II \hat{\mathbf{S}}^b) \right] \hat{\boldsymbol{\sigma}}. \quad (16)$$

Thus, the effective stiffness matrix \mathbf{C} can be expressed as

$$\mathbf{C} = \left[\hat{\mathbf{S}}^b + \frac{S}{V} (\hat{\mathbf{Z}}^I + \hat{\mathbf{Z}}^II \hat{\mathbf{S}}^b) \right]^{-1}. \quad (17)$$

The effective stiffness matrix of case of an inclined fracture can be obtained by rotating the coordinate axis to keep z-axis perpendicular to fracture interface. We define the inclined fracture have an angle φ and an azimuth angle θ , and then the rotation matrix can be obtained:

$$\hat{\mathbf{R}} = \begin{bmatrix} \cos \theta \cos \varphi & -\sin \theta & \cos \theta \sin \varphi \\ \sin \theta \cos \varphi & \cos \theta & \sin \theta \sin \varphi \\ -\sin \varphi & 0 & \cos \varphi \end{bmatrix}, \quad (18)$$

as well as the corresponding stress Bond matrix $\hat{\mathbf{A}}_\sigma(\hat{\mathbf{R}})$ and strain Bond matrix $\hat{\mathbf{A}}_\varepsilon(\hat{\mathbf{R}})$. The new stress matrix $\hat{\boldsymbol{\varepsilon}}'$ and strain matrix $\hat{\boldsymbol{\sigma}}'$ can be expressed as:

$$\hat{\boldsymbol{\varepsilon}}' = \hat{\mathbf{A}}_\varepsilon \hat{\boldsymbol{\varepsilon}}, \quad \hat{\boldsymbol{\sigma}}' = \hat{\mathbf{A}}_\sigma \hat{\boldsymbol{\sigma}}. \quad (19)$$

By substituting equation (19) into equation (13), the new exceed fracture strain matrix can be obtained

$$\hat{\boldsymbol{\varepsilon}}^c = \frac{S}{V} \hat{\mathbf{A}}_\varepsilon (\hat{\mathbf{Z}}^I + \hat{\mathbf{Z}}^II \hat{\mathbf{S}}^b) \hat{\mathbf{A}}_\sigma^T \hat{\boldsymbol{\sigma}}, \quad (20)$$

Finally, substituting equation (12) and (20) into equation (15), the average strain matrix of each numerical cell containing discrete distributed fractures with the same arbitrary direction can be expressed as

$$\hat{\mathbf{e}} = \left[\hat{\mathbf{S}}^b + \frac{S}{V} \hat{\mathbf{A}}_\varepsilon \left(\hat{\mathbf{Z}}^I + \hat{\mathbf{Z}}^{II} \hat{\mathbf{S}}^b \right) \hat{\mathbf{A}}_\varepsilon^T \right] \hat{\mathbf{g}}. \quad (21)$$

and the corresponding effective stiffness matrix \mathbf{C} is

$$\mathbf{C} = \left[\hat{\mathbf{S}}^b + \frac{S}{V} \hat{\mathbf{A}}_\varepsilon \left(\hat{\mathbf{Z}}^I + \hat{\mathbf{Z}}^{II} \hat{\mathbf{S}}^b \right) \hat{\mathbf{A}}_\varepsilon^T \right]^{-1}. \quad (22)$$

If the background media is isotropic, the \mathbf{C} can be simplified as

$$\mathbf{C} = \mathbf{C}^{iso} \left[\mathbf{I} + \frac{S}{V} \hat{\mathbf{A}}_\varepsilon \left(\hat{\mathbf{Z}}^I \mathbf{C}^{iso} + \hat{\mathbf{Z}}^{II} \right) \hat{\mathbf{A}}_\varepsilon^T \right]^{-1}. \quad (23)$$

If we ignore the interaction between different fractures and the FPD along the fracture interfaces, the result can be easily extended to the case of multiple sets of discrete distributed large-scale fractures with arbitrary orientation:

$$\mathbf{C} = \mathbf{C}^{iso} \left[\mathbf{I} + \sum_{r=1}^{N_c} \frac{S_r}{V} \hat{\mathbf{A}}_{\varepsilon r} \left(\hat{\mathbf{Z}}_r^I \mathbf{C}^{iso} + \hat{\mathbf{Z}}_r^{II} \right) \hat{\mathbf{A}}_{\varepsilon r}^T \right]^{-1}. \quad (24)$$

where N_c is total number of the fracture directions and the subscript r denotes the r th direction. The derived effective stiffness matrix is to be employed in the viscoelastic finite-difference modeling of discrete distributed large-scale fractures in porous rock.

Since the local effective medium theory assumes that the real structure of the fractured porous rock is substituted by ideal continua, the balance equations of classical continuum mechanics can be applied without considering the discontinuity at the fracture interfaces, and the constitutive equations can be characterized by the effective viscoelastic stiffness. Combined with the effective complex-valued and frequency-dependent TTI viscoelastic stiffness, the 2-D frequency-domain second-order heterogeneous governing equations with PML of fractured porous rock can be expressed as:

$$\begin{aligned} \omega^2 \rho u_x + \frac{1}{\xi_x} \partial_x \left(\frac{c_{11}}{\xi_x} \partial_x u_x + \frac{c_{13}}{\xi_z} \partial_z u_z + \frac{c_{15}}{\xi_z} \partial_z u_x + \frac{c_{15}}{\xi_x} \partial_x u_z \right) + \frac{1}{\xi_z} \partial_z \left(\frac{c_{15}}{\xi_x} \partial_x u_x + \frac{c_{35}}{\xi_z} \partial_z u_z + \frac{c_{55}}{\xi_z} \partial_z u_x + \frac{c_{55}}{\xi_x} \partial_x u_z \right) &= 0, \\ \omega^2 \rho u_z + \frac{1}{\xi_x} \partial_x \left(\frac{c_{15}}{\xi_x} \partial_x u_x + \frac{c_{35}}{\xi_z} \partial_z u_z + \frac{c_{55}}{\xi_z} \partial_z u_x + \frac{c_{55}}{\xi_x} \partial_x u_z \right) + \frac{1}{\xi_z} \partial_z \left(\frac{c_{13}}{\xi_x} \partial_x u_x + \frac{c_{33}}{\xi_z} \partial_z u_z + \frac{c_{35}}{\xi_z} \partial_z u_x + \frac{c_{35}}{\xi_x} \partial_x u_z \right) &= 0, \end{aligned} \quad (25)$$

where u_x and u_z are the horizontal and vertical components of particle displacement vector, ρ is the effective density, and c_{ij} are the components of complex-valued and frequency-dependent effective stiffness matrix, ξ_x and ξ_z are the frequency domain PML damping functions.

In time domain, the governing equations are integral differential equations, which require special processing for the convolution operations, resulting in high computational costs. Although the problem can be relieved by memory functions, it still requires high memory requirements. Instead, the governing equations can be straightforwardly solved using FDFD. To efficiently and accurately modelling of seismic wave propagation in fluid saturated fractured porous rock, we solve the second-order heterogeneous governing equations with mixed-grid stencil FDFD method (Jo et al., 1996; Hustedt et al. 2004). The mixed system of governing equations is formulated by combining the classical Cartesian coordinate system (CS) and the 45°-rotated coordinate system (RS):

$$\begin{aligned} \omega^2 \rho u_x + w_1 (A_c u_x + B_c u_z) + (1 - w_1) (A_r u_x + B_r u_z) &= 0, \\ \omega^2 \rho u_z + w_1 (C_c u_x + D_c u_z) + (1 - w_1) (C_r u_x + D_r u_z) &= 0, \end{aligned} \quad (26)$$

where the optimal averaging coefficient $w_1 = 0.5461$ (Jo et al., 1996). The coefficients A_c, B_c, C_c, D_c and A_r, B_r, C_r, D_r are functions of the damping functions, effective stiffness coefficients and spatial derivative operators and the detailed expressions are given in Appendix A. We follow Hustedt et al., (2004) and Liu et al., (2018) to discretize the derivative operation on the mixed systems using mixed grid stencil. After discretization and arrangement, the mixed system of governing equations can be written in matrix form as

$$\begin{bmatrix} \mathbf{M} + w_1 \mathbf{A}_c + (1 - w_1) \mathbf{A}_r & w_1 \mathbf{B}_c + (1 - w_1) \mathbf{B}_r \\ w_1 \mathbf{C}_c + (1 - w_1) \mathbf{C}_r & \mathbf{M} + w_1 \mathbf{D}_c + (1 - w_1) \mathbf{D}_r \end{bmatrix} \begin{bmatrix} \mathbf{u}_x \\ \mathbf{u}_z \end{bmatrix} = \begin{bmatrix} \mathbf{0} \\ \mathbf{0} \end{bmatrix}, \quad (27)$$

where \mathbf{M} denotes the diagonal mass matrix of coefficients $\omega^2 \rho$, and blocks $\mathbf{A}_c, \mathbf{B}_c, \mathbf{C}_c, \mathbf{D}_c$ and $\mathbf{A}_r, \mathbf{B}_r, \mathbf{C}_r, \mathbf{D}_r$ form the stiffness matrices for the CS and RS stencils, respectively, and the corresponding coefficients of submatrices are given in Appendix B.

To improve the modelling accuracy of mixed-grid stencil, the acceleration term $\omega^2 \rho$ are approximated using a weighted average over the mixed operator stencil nodes:

$$[\omega^2 \rho]_{ij} \approx \omega^2 \left[w_{m1} \rho_{ij} + w_{m2} (\rho_{i+1,j} + \rho_{i-1,j} + \rho_{i,j+1} + \rho_{i,j-1}) + w_{m3} (\rho_{i+1,j+1} + \rho_{i-1,j-1} + \rho_{i-1,j+1} + \rho_{i+1,j-1}) \right], \quad (28)$$

where the optimal coefficients $w_{m1} = 0.6248$, $w_{m2} = 0.09381$ and $w_{m3} = (1 - w_{m1} - 4w_{m2})/4$ are computed by Jo et al. (1996).

In order to assess the FPD effects on seismic response, a similar procedure can be adopted in the implementation of elastic modeling by replacing the frequency-dependent fracture compliances with its low- or high-frequency limit compliances. The main advantage of our VLSM-based modeling scheme over poroelastic modeling schemes is that the fractured domain can be modeled using a viscoelastic solid, while the rest of the domain can be modeled using an elastic solid.

3.2 Poroelastic modeling based on PLSM

The poroelastic modeling means that we numerically solve the Biot's equations and adopt an explicit implementation of the PLSM across each fracture instead of using the effective media theory. Hence, the poroelastic modeling can naturally deal with the FPD between fracture and background and account for its impact on wave scattering. To verify the effectiveness of the viscoelastic modeling based on VLSM, we compared the results obtained from viscoelastic scheme with those obtained from the poroelastic scheme. Although it is difficult to implement an explicit application of PLSM for arbitrary orientated fracture, it is relatively straightforward for horizontal or vertical fracture. In the following text, we outline the poroelastic modeling for a single horizontal fracture embedded in an isotropic homogeneous background with an explicit implementation of the PLSM. In frequency domain, the governing equations for an isotropic poroelastic media in the absent of fractures can be written as (Biot, 1962):

$$\begin{aligned}
& -\omega^2 \rho u_i - \omega^2 \rho_f w_i = \partial_i \sigma_{ij}, \\
& -\omega^2 \rho_f u_i - \omega^2 \rho_w w_i + i\omega \frac{\eta}{\kappa} w_i = -\partial_i P_f, \\
& \sigma_{ij} = (H_U - 2\mu) \partial_i u_j + \alpha M \partial_i w_j + \mu (\partial_j u_i + \partial_i u_j), \\
& -P_f = \alpha M \partial_i u_i + M \partial_i w_i.
\end{aligned} \tag{29}$$

In the presence of fractures, the spatial derivative of stress remains unchanged. However, due to the discontinuity of particle displacements across the fracture interface, its spatial derivative consists of two parts, i.e. the background and the fracture:

$$\begin{aligned}
\frac{\partial u_x}{\partial z} &= \left(\frac{\partial u_x}{\partial z} \right)_{BG} + \left(\frac{\partial u_x}{\partial z} \right)_{FR}, \\
\frac{\partial u_z}{\partial z} &= \left(\frac{\partial u_z}{\partial z} \right)_{BG} + \left(\frac{\partial u_z}{\partial z} \right)_{FR}, \\
\frac{\partial w_z}{\partial z} &= \left(\frac{\partial w_z}{\partial z} \right)_{BG} + \left(\frac{\partial w_z}{\partial z} \right)_{FR}.
\end{aligned} \tag{30}$$

The spatial derivative of the background is described by the equation (29):

$$\begin{aligned}
\left(\frac{\partial u_x}{\partial x} \right)_{BG} &= \frac{H_D}{4\mu(H_D - \mu)} \sigma_{xx} - \frac{H_D - 2\mu}{4\mu(H_D - \mu)} \sigma_{zz} + \frac{2\alpha\mu}{4\mu(H_D - \mu)} P_f, \\
\left(\frac{\partial u_z}{\partial z} \right)_{BG} &= -\frac{H_D - 2\mu}{4\mu(H_D - \mu)} \sigma_{xx} + \frac{H_D}{4\mu(H_D - \mu)} \sigma_{zz} + \frac{2\alpha\mu}{4\mu(H_D - \mu)} P_f, \\
\left(\frac{\partial w_x}{\partial x} + \frac{\partial w_z}{\partial z} \right)_{BG} &= -\frac{2\alpha\mu}{4\mu(H_D - \mu)} \sigma_{xx} - \frac{2\alpha\mu}{4\mu(H_D - \mu)} \sigma_{zz} - \frac{H_U - \mu}{M(H_D - \mu)} P_f.
\end{aligned} \tag{31}$$

The fracture induced spatial derivative can be obtained based on the PLSM:

$$\begin{aligned}
\left(\frac{\partial u_x}{\partial z} \right)_{FR} &= \frac{\Delta u_x}{\Delta z} = \frac{Z_T}{\Delta z} \sigma_{xz}, \\
\left(\frac{\partial u_z}{\partial z} \right)_{FR} &= \frac{\Delta u_z}{\Delta z} = \frac{Z_{N_D}}{\Delta z} (\sigma_{zz} + \alpha P_f), \\
\left(\frac{\partial w_z}{\partial z} \right)_{FR} &= \frac{\Delta w_z}{\Delta z} = -\frac{Z_{N_D}}{\Delta z} \left(\alpha \sigma_{zz} + \frac{H_U}{M} P_f \right).
\end{aligned} \tag{32}$$

By substituting equation (31)-(32) into equation (30) and rewritten equation (29), we obtain the governing equations for numerical simulation of elastic wave in fractured poroelastic media in matrix form:

$$-\omega^2 \hat{\mathbf{R}} \hat{\mathbf{u}} = \nabla \hat{\mathbf{S}}^{-1} \nabla^T \hat{\mathbf{u}}, \tag{33}$$

where $\hat{\mathbf{u}} = (u_x, u_z, w_x, w_z)^T$ is the displacement vector, $\hat{\mathbf{R}}$, $\hat{\mathbf{S}}$ and ∇ are the density, compliance and spatial derivative matrix, respectively. The three matrices in equation (33) are defined as:

$$\hat{\mathbf{R}} = \begin{bmatrix} \rho & 0 & \rho_f & 0 \\ 0 & \rho & 0 & \rho_f \\ \rho_f & 0 & \rho_m & 0 \\ 0 & \rho_f & 0 & \rho_m \end{bmatrix}, \quad \left(\rho_m = \rho_w - \frac{i\eta}{\omega\kappa} \right). \tag{34}$$

$$\nabla = \begin{bmatrix} \partial_x & 0 & \partial_z & 0 \\ 0 & \partial_z & \partial_x & 0 \\ 0 & 0 & 0 & \partial_x \\ 0 & 0 & 0 & \partial_z \end{bmatrix}, \quad (35)$$

$$\hat{\mathbf{S}} = \begin{bmatrix} \frac{H_D}{4\mu(H_D - \mu)} & -\frac{H_D - 2\mu}{4\mu(H_D - \mu)} & 0 & -\frac{2\alpha\mu}{4\mu(H_D - \mu)} \\ -\frac{H_D - 2\mu}{4\mu(H_D - \mu)} & \frac{H_D}{4\mu(H_D - \mu)} + \frac{Z_{N_D}}{\Delta z} & 0 & -\frac{2\alpha\mu}{4\mu(H_D - \mu)} - \frac{\alpha Z_{N_D}}{\Delta z} \\ 0 & 0 & \frac{1}{\mu} + \frac{Z_T}{\Delta z} & 0 \\ -\frac{2\alpha\mu}{4\mu(H_D - \mu)} & -\frac{2\alpha\mu}{4\mu(H_D - \mu)} - \frac{\alpha Z_{N_D}}{\Delta z} & 0 & -\frac{H_U - \mu}{M(H_D - \mu)} - \frac{H_U Z_{N_D}}{M \Delta z} \end{bmatrix}. \quad (36)$$

A compact discretized wave equation system that contains only displacement field can be obtained by using second-order difference operators to discretize the new governing equations:

$$\begin{bmatrix} \mathbf{G}_{11} & \mathbf{G}_{12} & \mathbf{G}_{13} & \mathbf{G}_{14} \\ \mathbf{G}_{21} & \mathbf{G}_{22} & \mathbf{G}_{23} & \mathbf{G}_{24} \\ \mathbf{G}_{31} & \mathbf{G}_{32} & \mathbf{G}_{33} & \mathbf{G}_{34} \\ \mathbf{G}_{41} & \mathbf{G}_{42} & \mathbf{G}_{43} & \mathbf{G}_{44} \end{bmatrix} \begin{bmatrix} \mathbf{u}_x \\ \mathbf{u}_z \\ \mathbf{w}_x \\ \mathbf{w}_z \end{bmatrix} = \begin{bmatrix} \mathbf{0} \\ \mathbf{0} \\ \mathbf{0} \\ \mathbf{0} \end{bmatrix}, \quad (37)$$

where blocks $\mathbf{G}_{i,j}$ ($i, j = 1 \dots 4$) forms the stiffness matrices of the discretized system of the poroelastic wave equations. The poroelastic modeling based on PLSM will be used to validate the other modeling schemes.

4 Numerical examples

Table1 Physical Properties of the Materials Employed in the Numerical Modeling

Parameters	Background	Fracture	Underlying
Porosity, ϕ	0.15	0.8	0.05
Permeability, κ	0.1 D	100 D	0.01 D
Solid bulk modulus, K_s	36 GPa	36 GPa	36 GPa
Frame bulk modulus, K_m	20.3 GPa	0.055 GPa	30.6 GPa
Frame shear modulus, μ_m	18.6 GPa	0.033 GPa	32.2 GPa
Solid density, ρ_s	2700 kg/m ³	2700 kg/m ³	2700 kg/m ³
Fluid density, ρ_f	1000 kg/m ³	1000 kg/m ³	1000 kg/m ³
Fluid shear viscosity, η_f	0.01 Poise	0.01 Poise	0.01 Poise
Fluid bulk modulus, K_f	2.25 GPa	2.25 GPa	2.25 GPa
Thickness, h		1 mm	

In this section, we apply different numerical modeling schemes on three fractured models to examine the FPD effects on seismic wave scattering. We mainly focus on the amplitudes and phases of the scattered and reflected waves.

4.1 Single fracture model

Here, we numerically simulate the scattering of seismic waves from a single fracture embedded in a homogeneous background. The model measures $2000m \times 1500m$ with a grid interval 5m (namely, the numerical grids size is 401×301) surrounded by a

200m thick PML boundary. The fracture is parallel to the x -axis (a horizontal fracture) and located 750m directly below the source (1000m, 30m), with a 500m horizontal extending. A Ricker wavelet with a central frequency of 35Hz is used as the temporal source excitation. The material properties of the fracture and background are given in Table 1 modified from Nakagawa and Schoenberg (2007) and Barbosa et al. (2016a). For comparison, we present the seismic wavefields obtained using the poroelastic modeling based on PLSM, the viscoelastic modeling based on VLSM, as well as the elastic modeling based on low-frequency limit of VLSM (LVLSM) and high-frequency limit of VLSM (HVLSM). For the convenience of observation of the impact of the FPD on the scattered P - and S -wave of the fracture, we apply the pressure source in all four schemes.

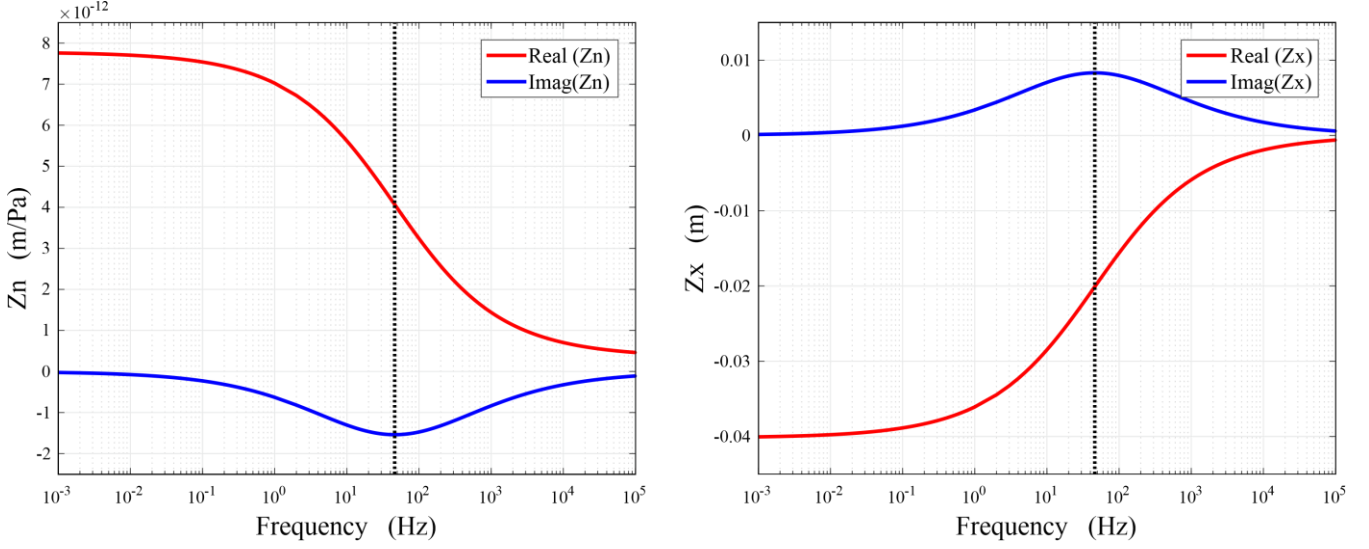


Figure 1: Complex-valued and frequency-dependent Z_N and Z_X . The dashed vertical line denotes the characteristic frequency computed using equation (8).

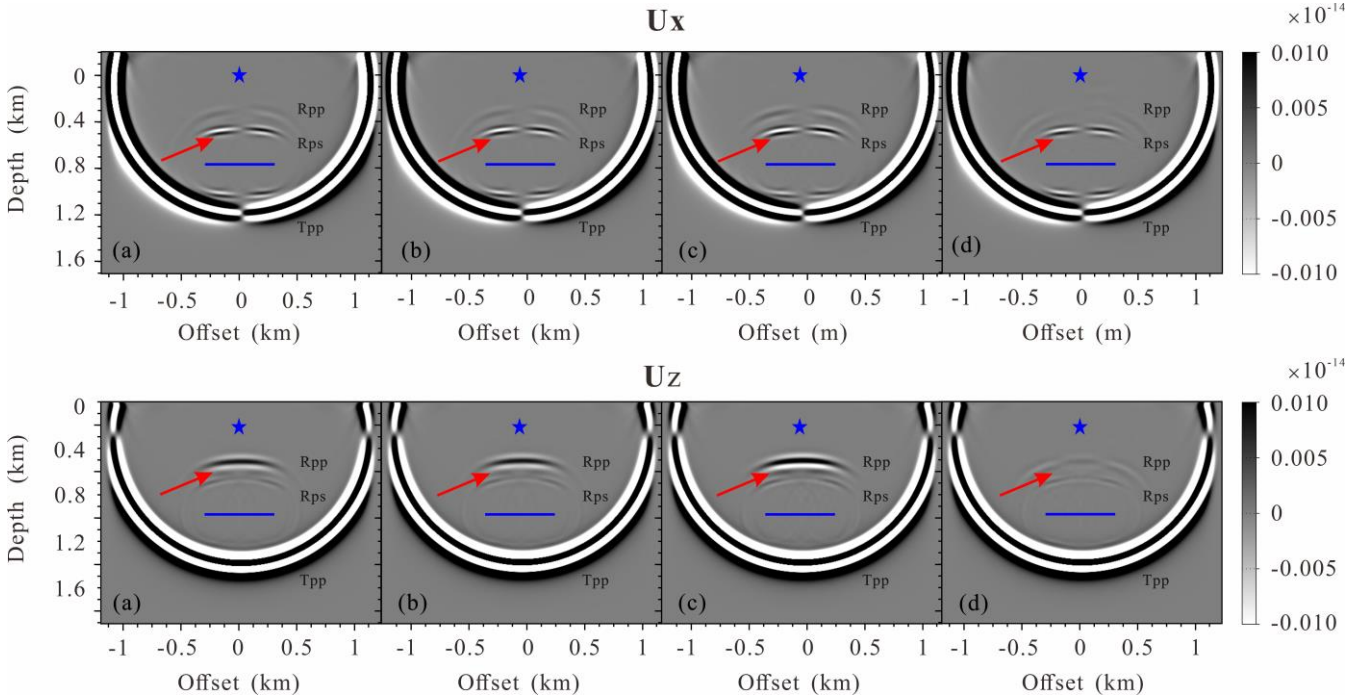


Figure 2: Snapshots of the wavefields components U_x and U_z for a single horizontal fracture model at 280ms: (a) the PLSM based poroelastic modeling, (b) the VLSM based viscoelastic modeling, (c) the LVLSM based elastic modeling and (d) the HVLSM based elastic modeling. The blue asterisk and line represent the source and the fracture, respectively.

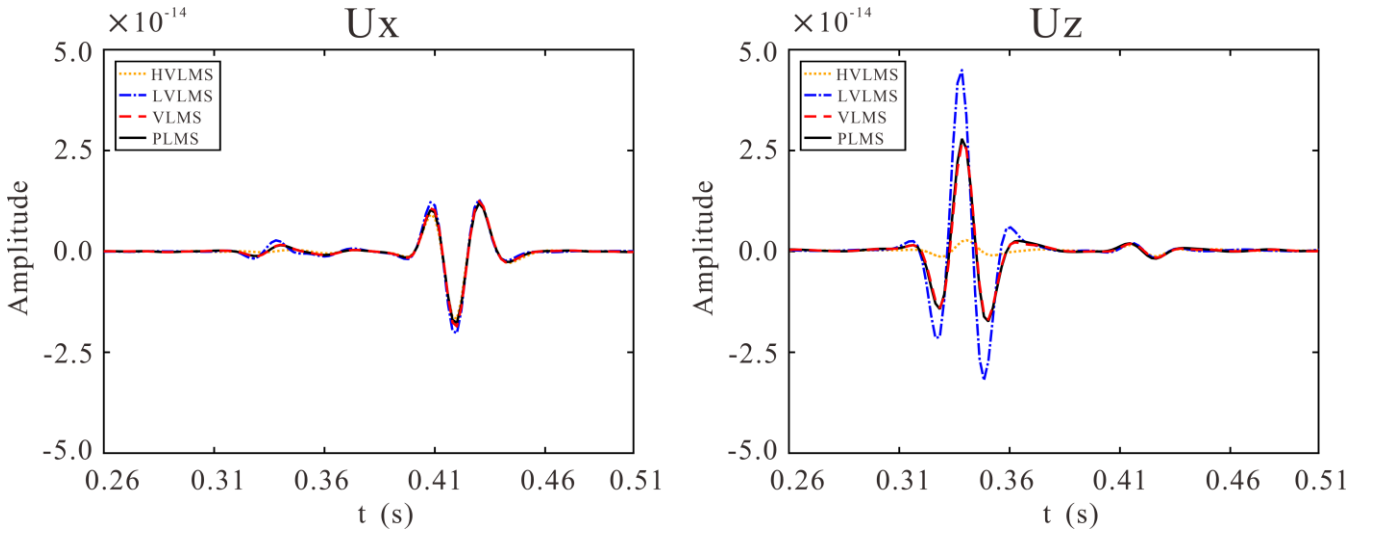


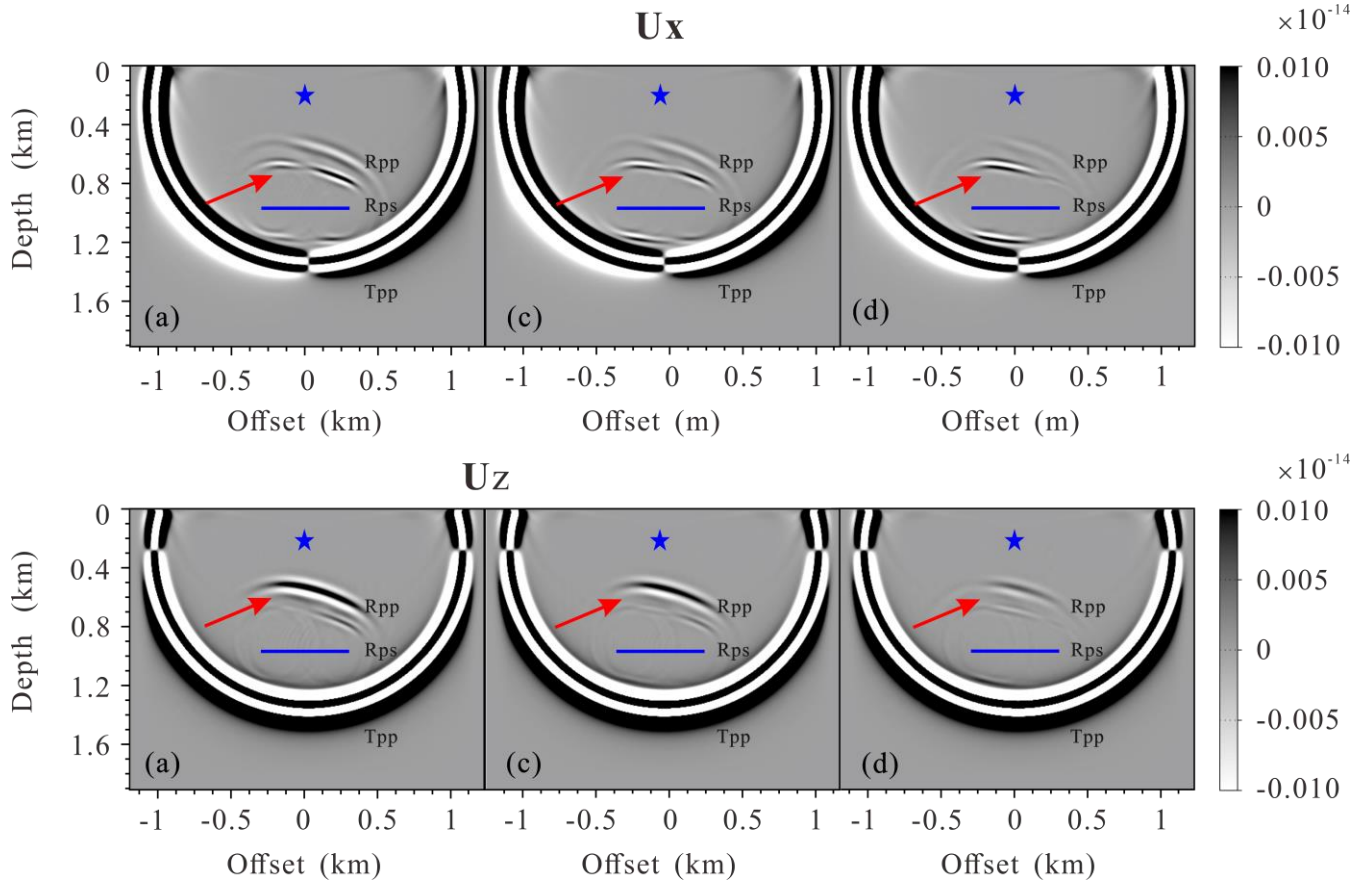
Figure 3: Comparison of 1-D seismograms components U_x and U_z at (1200m, 0m) for a single horizontal fracture model.

Figure 1 shows the complex-valued and frequency-dependent fracture normal compliance Z_N and dimensionless parameter Z_x computed from equation (6). The mechanical compliance of the fracture is strongly controlled by FPD effects. It can be observed that the real part of the fracture normal compliance decreases with the increment of frequency, while the imaginary part has a peak at the characteristic frequency, corresponding to the maximal dispersion. The central frequency (35Hz) of the Ricker wavelet used for numerical simulation is close to the characteristic frequency (46Hz), which ensures that the impact of the FDP effects on seismic scattering is significant in the seismic frequency band.

Figure 2 shows the 280ms snapshots of the displacement fields for the single horizontal fracture model models. The displacement fields are calculated by the PLSM-based poroelastic modeling, the VLMSM-based viscoelastic modeling, the LVLMSM-based elastic modeling and the HVLMSM-based elastic modeling, respectively. The asterisk represents the source and the blue line represents the fracture. To make the small scattered wave visible, large amplitude is clipped, thus the transmitted compressional waves (T_{PP}), scattered compressional waves (S_{PP}) and scattered converted waves (S_{PS}) can be seen clearly. It should note that the slow P -waves are invisible in the poroelastic modeling, due to the high diffusion and attenuation of slow P -waves in the background media. Figure 3 present the comparison of 1-D seismograms at (1200m, 0m).

We consider the poroelastic modeling as a reference scenario because it can naturally incorporate the FPD effects. Figure 2 and Figure 3 suggest very good agreement between the S_{PP} amplitude calculated using the PLSM-based and VLMSM-based modeling, while the HVLMSM-based modeling obviously underestimate the S_{PP} amplitude, and the LVLMSM-based modeling overestimate the S_{PP} amplitude. This is to be expected, since the scattering behavior of a fracture is mainly controlled by the stiffness contrast with respect to the background. The HVLMSM assumes there is insufficient time for fluid exchange at the fracture interface, the fracture behaves as being sealed and the stiffness of the saturated fracture is maximal, resulting in an underestimated stiffness contrast between fracture and background. The LVLMSM assumes there is enough time for fluid flow between the fracture and background, the deformation of the fracture is maximal, resulting in an overestimated stiffness contrast with background. The VLMSM derived from poroelastic theory, however, can properly incorporate the FPD effects,

339 leading to a frequency-dependent stiffness contrast equivalent to the PLSM. It can be note that the S_{PP} amplitudes obtained
 340 using the LVLSM-based modeling is comparable to that of the PLSM based modeling, because the FPD effects mainly occur
 341 at seismic frequencies closer to the low frequency limit. The S_{PP} travel time obtained using the four modeling schemes shows
 342 good consistency. Figure 2 and Figure 3 also show that the discrepancy of the S_{PS} amplitudes is almost negligible. Because the
 343 S -wave scattering behavior is mainly controlled by the drained stiffness contrast between the fracture and the background. The
 344 comparison of different modeling schemes demonstrates that the DLSM-based viscoelastic modeling can appropriately capture
 345 the FPD effects on wave scattering of a fluid saturated fracture, while the two elastic modeling cannot correctly estimate the
 346 scattered waves.



347
 348 **Figure 4: Snapshots of the wavefields components U_x and U_z for a single inclined fracture model at 280ms: (a) the PLSM based**
 349 **poroelastic modeling, (b) the VLSM based viscoelastic modeling, (c) the LVLSM based elastic modeling and (d) the HVLSM based**
 350 **elastic modeling. The blue asterisk and line represent the source and the fracture, respectively.**

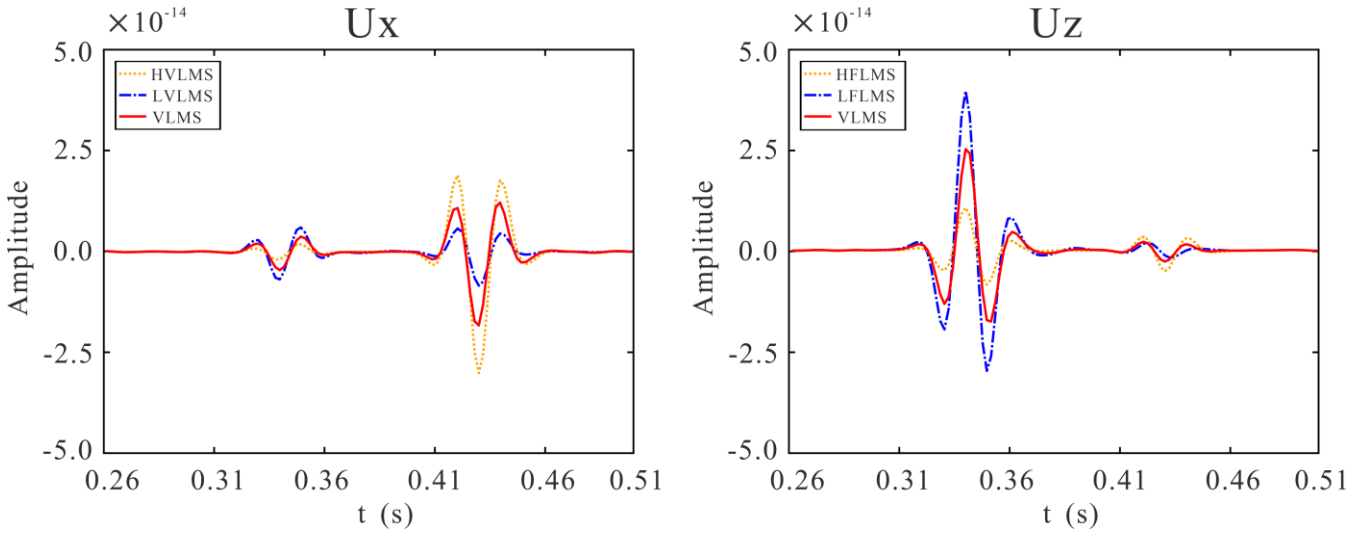


Figure 5: Comparison of 1-D seismograms components Ux and Uz at (1000m, 0m) for a single inclined fracture model.

The proposed modeling scheme is also applicable to the inclined fracture. Figure 4 shows the 280ms snapshots of the displacement fields for the single inclined fracture model models. Figure 5 is the comparison of 1-D seismograms at (1200m,0m). Figure 4 and Figure 5 show that both the scattered *P*- and *S*-waves of a single inclined fracture are strongly affected by the FPD effects.

4.2 Fractured reservoir model

In addition to a single fracture, we are more interested in the scattering behavior of discrete distributed fractures system. To this end, we designed two fractured reservoir models containing a set of regularly distributed aligned horizontal fractures and a set of randomly distributed aligned horizontal fractures, respectively, as illustrated in Figure 6. There are 200 horizontal fractures spread over a space of 200m, each extending 500m. The material properties of the fracture, background (yellow region) and underlying (green region) formation are given in Table 1. The model size, grid interval and source location are the same as those in the previous numerical examples. Through a set of aligned horizontal fracture structures is not practical in the actual subsurface, it helps to illustrate the impact of FPD effects on the amplitude and phase of scattered waves of fractures.

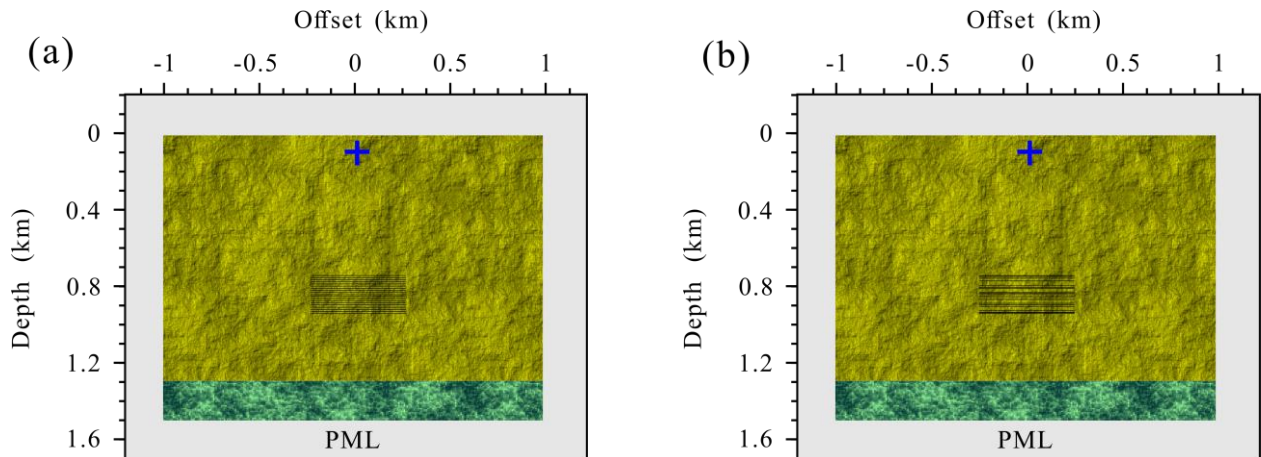


Figure 6: Schematic diagram of the fractured reservoir model with a set of aligned horizontal fractures: (a)regular distribution (b)random distribution. The black segments present the fracture system. The extending of each fracture is 500m.

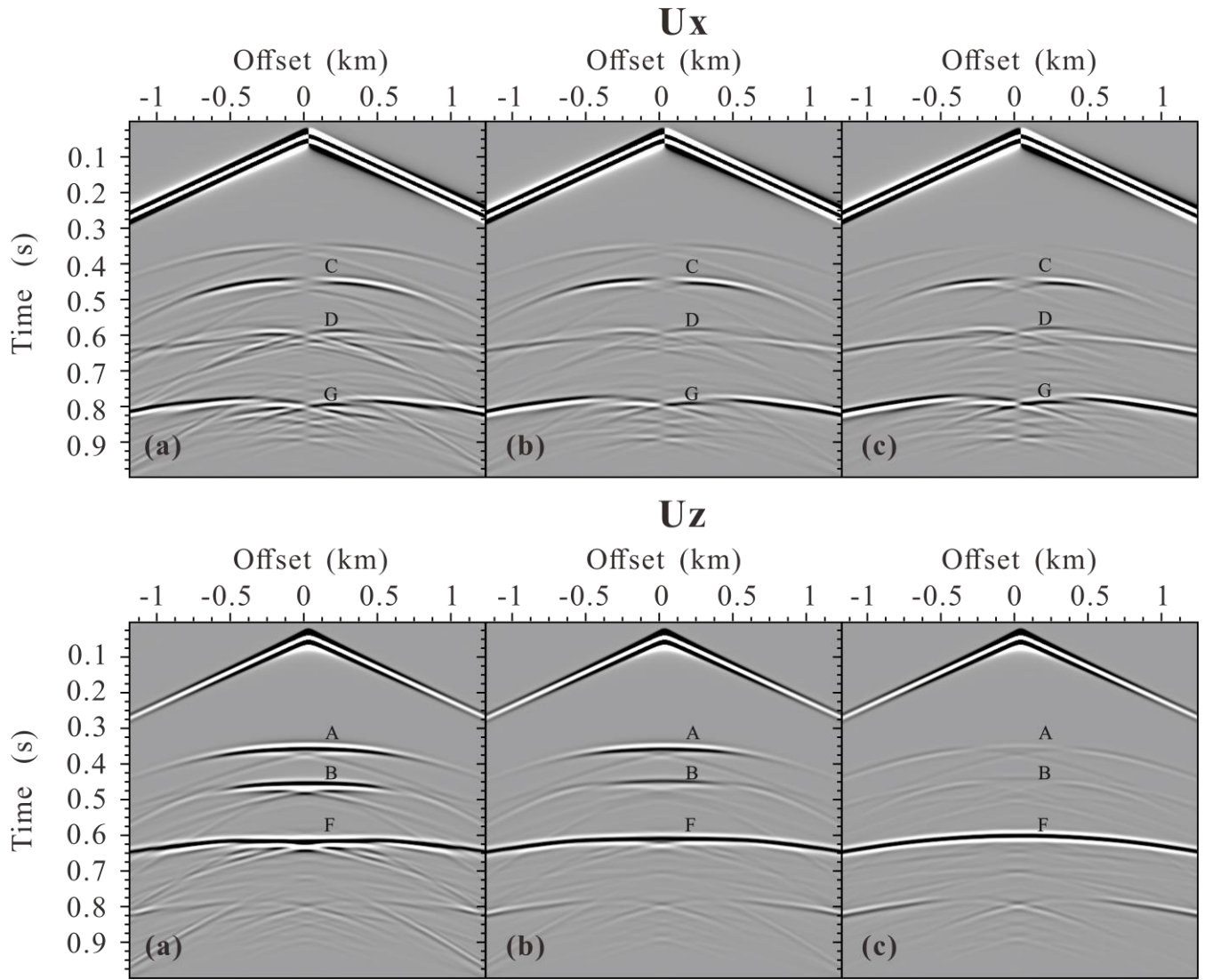


Figure 7: Seismogram components U_x and U_z of the fractured reservoir model with a set of regularly distributed aligned horizontal fractures calculated using (a) the LVLSM, (b) the VLISM, (c) the HVLSM. A, B are scattered P -wave from top and bottom, respectively, C and D are scattered converted shear S -wave from top and bottom, respectively, F and G are reflected P -wave and shear converted S -wave, respectively.

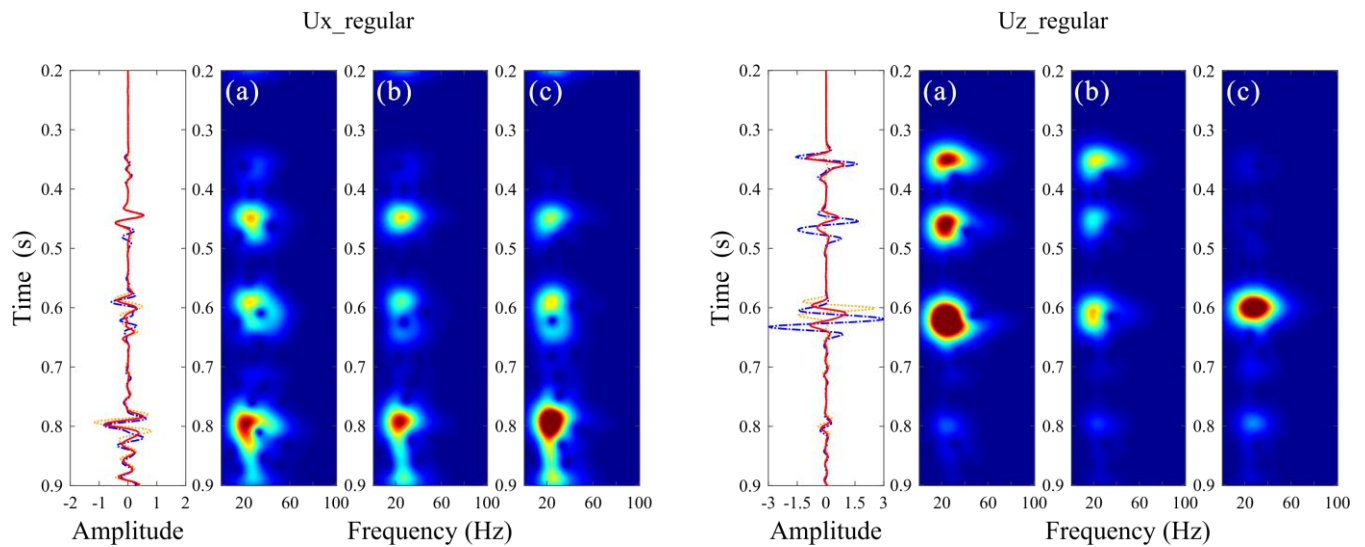


Figure 8: Time-frequency distributions of the middle trace for (b) the LVPLM, (c) the PLSM, and (d) the HVLSM cases in Figure 7.

Figure 7 presents the seismograms of fractured reservoir model with a set of regular distributed aligned horizontal fractures. The scattered compressional wave (S_{PP}) and scattered converted wave (S_{PS}) from the top and bottom of the fractured reservoir, the reflected compressional wave (R_{PP}), converted wave (R_{PS}) from the underlying formation can be clearly identified. Due to the regular distribution of aligned fracture, the fractured reservoir is equivalent to an anisotropic homogeneous media, and therefore the diffracted wave is generated only at the edges of the fractured reservoir. Similar to the single fracture case, the amplitude of the S_{PP} from the top and bottom of the fractured reservoir obtained by the HVLSM-based modeling is weakest (underestimated), that obtained by LVLSM-based modeling is strongest (overestimated), and that obtained by the VLSM-based modeling is intermediate. We notice that the S_{PP} amplitudes from the bottom of the fractured reservoir obtained by the LVLSM-based and HVLSM-based modeling are slightly smaller than those from the top, while the S_{PP} amplitude from the bottom obtained by the VLSM-based modeling is much smaller than that from the top. This is expected, since the VLSM-based modeling scheme can capture the wave attenuation and dispersion due to the FDP effects between the fracture system and background, while the LVLSM and HVLSM represent non-attenuated and non-dispersive elastic processes. Another evidence for attenuation is that the R_{PP} amplitudes of underlying formation calculated by the HVLSM-based and LVLSM-based modeling are almost equal, while the R_{PP} amplitude calculated by the VLSM-based modeling is much smaller. Figure 7 also shows that the arrival times of S_{PP} from the bottom and R_{PP} from underlying formation obtained by the three modeling schemes are different.

To show the trend of frequency-dependent attenuation and dispersion, time-frequency distribution of the middle trace was computed for three modeling schemes. Figure 8 clearly shows that the frequency content and energy of the scattered and reflected waves calculated by VLSM tend to decrease strongly, while the frequency content and energy calculated by HVLSM and LVLSM remain steady. The impact of FPD effects on the S_{PS} and R_{PS} is similar to that of the S_{PP} and R_{PP} , but to a much weaker extent.

In addition to regularly distributed fractures, our proposed modeling scheme can also simulate the wave scattering of random distributed fractures. Figure 9 presents the seismograms of fractured reservoir model with a set of random distributed aligned horizontal fractures. Figure 10 presents the time-frequency distributions of the middle trace for three modeling schemes cases in Figure 9. Due to the random distribution of aligned fracture, the fractured reservoir exhibits a stronger heterogeneity, resulting in more prevalent diffracted wave (coda wave) in Figure 9 than in Figure 7. Except for the diffracted wave, the scattered and reflected waves in the random distribution case is similar to those in the regular distribution case due to the FPD effect. The two fractured reservoir models suggest that the scattered waves from the bottom of the fractured reservoir are attenuated and dispersed by the FPD effects and the reflected waves can retain the relevant attenuation and dispersion information.

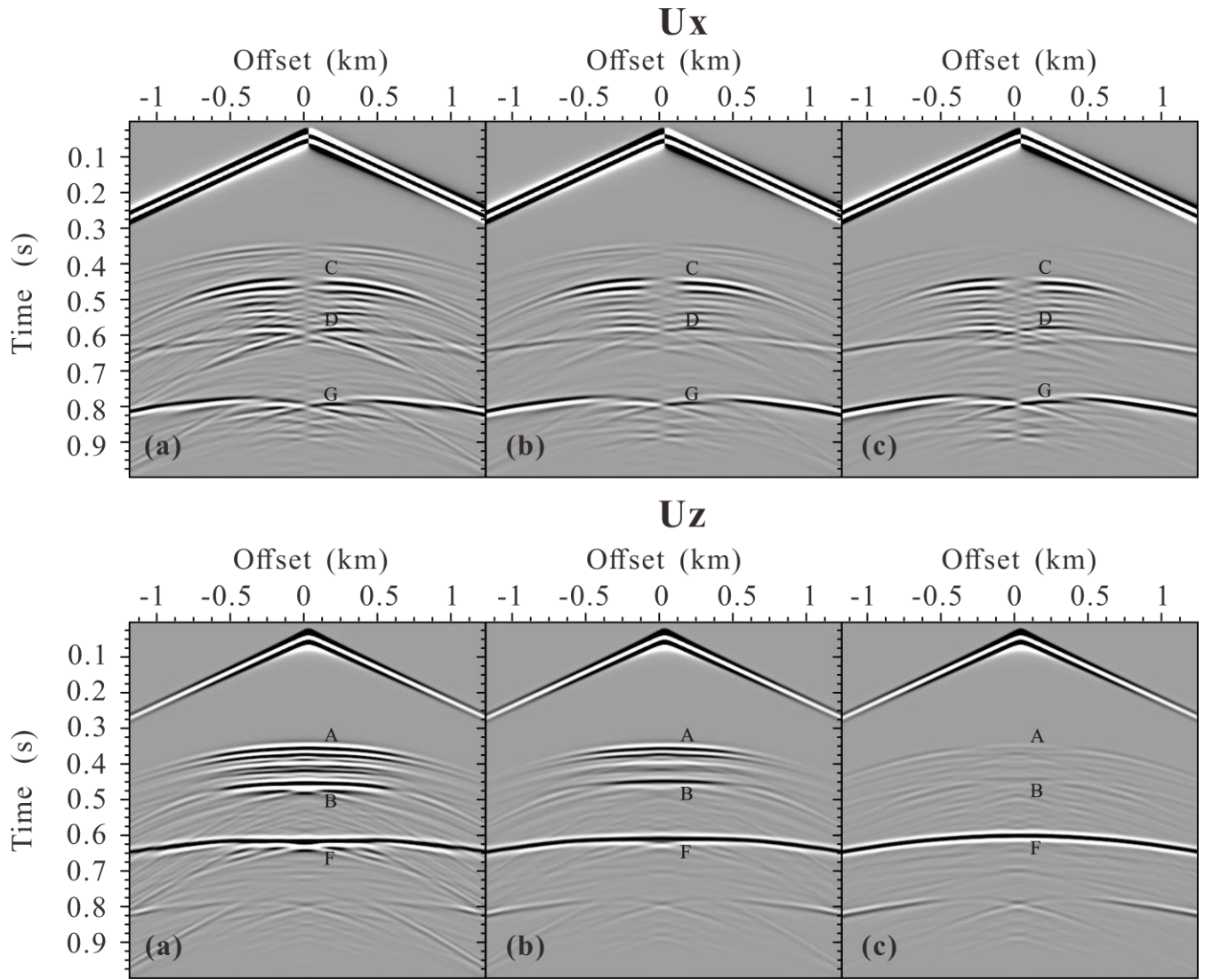


Figure 9: Seismogram components U_x and U_z of the fractured reservoir model with a set of randomly distributed aligned horizontal fractures calculated using (a) the LVLSM, (b) the VLSM, (c) the HVLSM. A, B are scattered P -wave from top and bottom, respectively, C and D are scattered converted shear S -wave from top and bottom, respectively, F and G are reflected P -wave and shear converted S -wave, respectively.

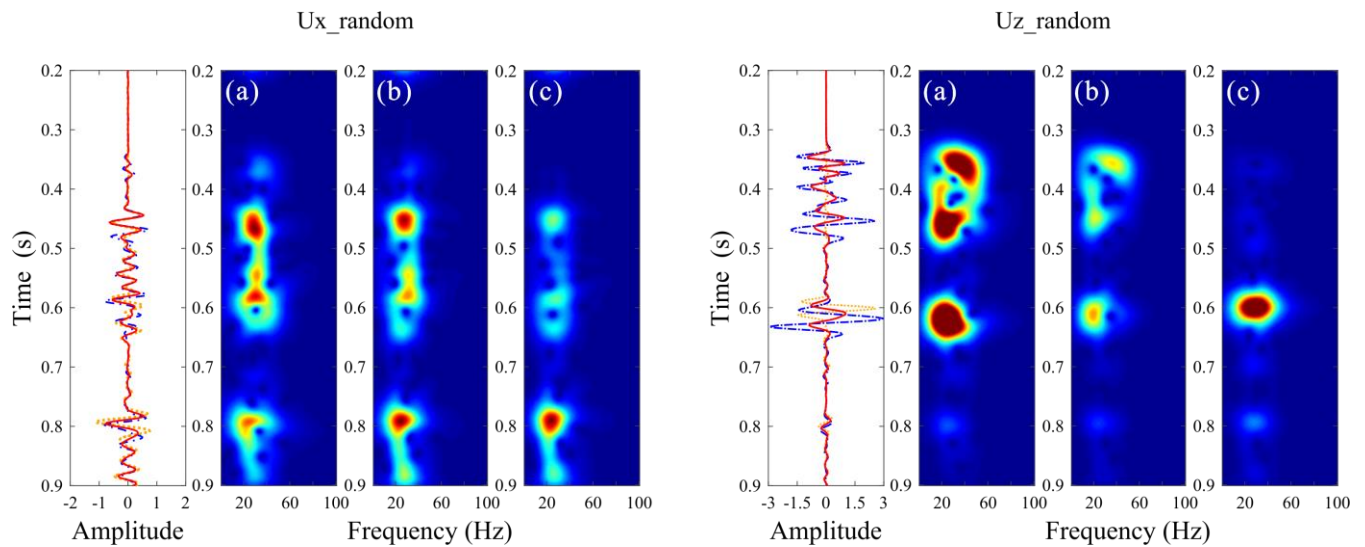


Figure 10: Time-frequency distributions of the middle trace for (b) the LVPLM, (c) the PLSM, and (d) the HVLSM cases in Figure 9.

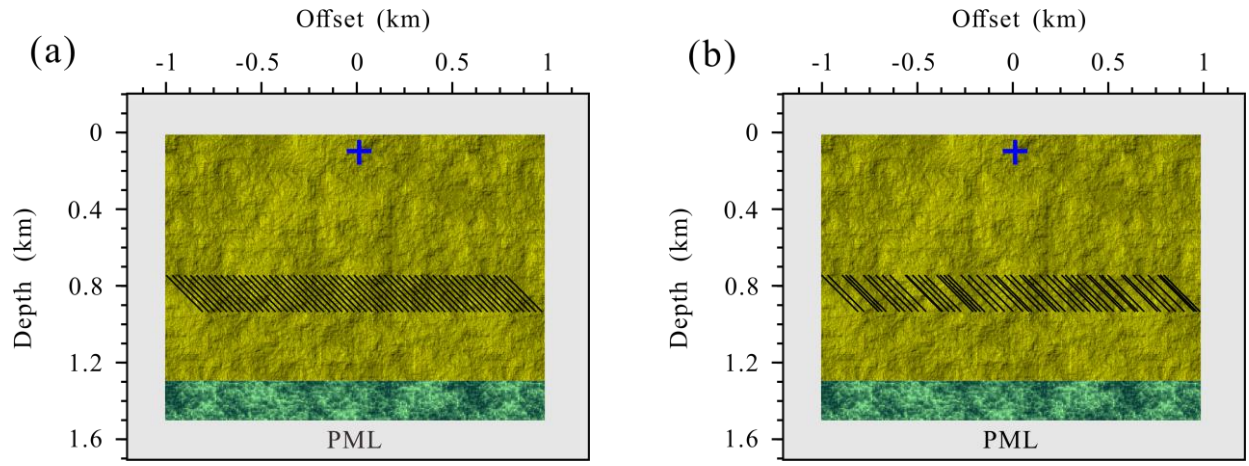


Figure 11: Schematic diagram of the fractured reservoir model with a set of aligned inclined fractures: (a) regular distribution (b) random distribution. The black segments present the fracture system. The extending of each fracture is 282.8m.

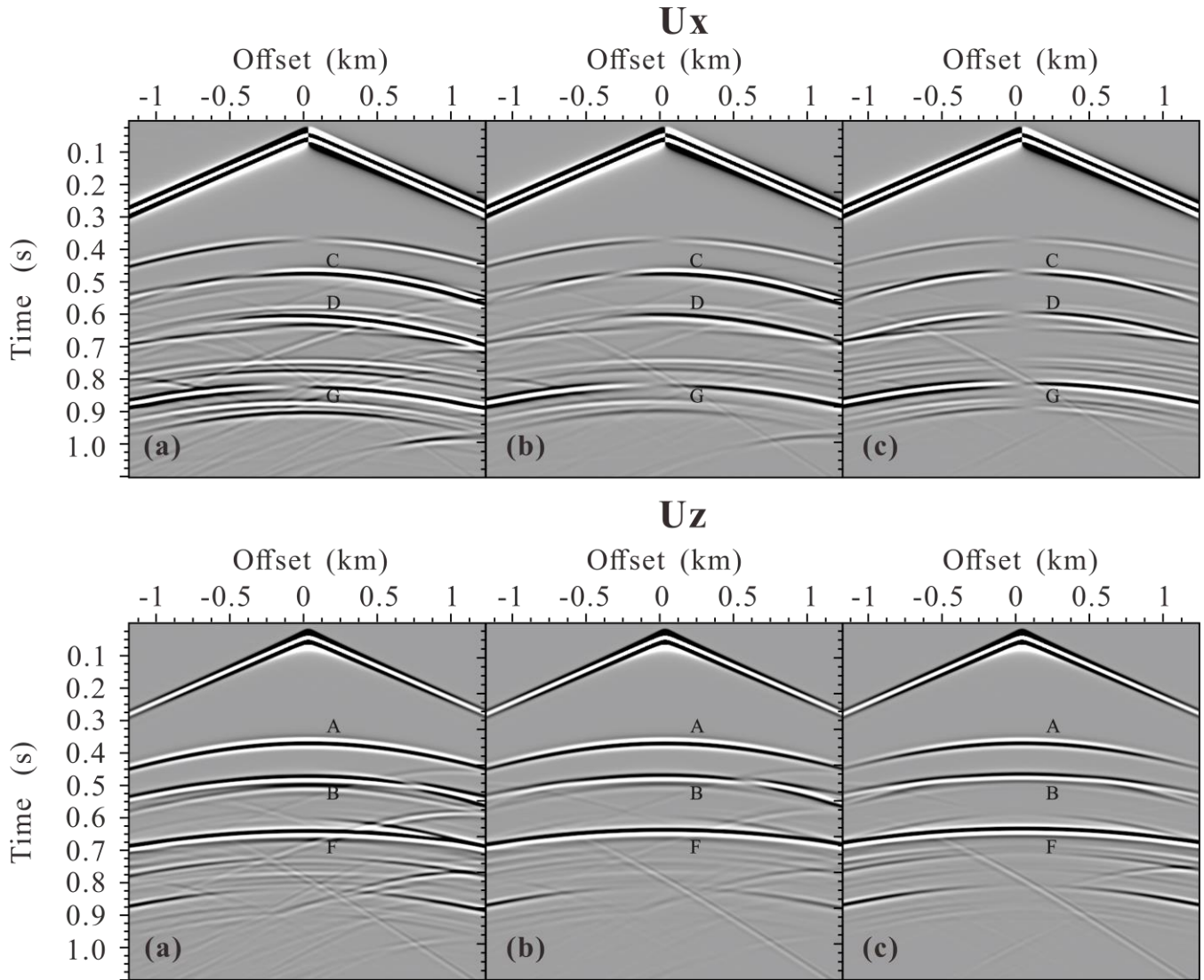


Figure 12: Seismogram components U_x and U_z of the fractured reservoir model with a set of regularly distributed aligned inclined fractures calculated using (a) the LVLSM, (b) the VLSM, (c) the HVLMS. A, B are scattered P -wave from top and bottom, respectively, C and D are scattered converted shear S -wave from top and bottom, respectively, F and G are reflected P -wave and shear converted S -wave, respectively.

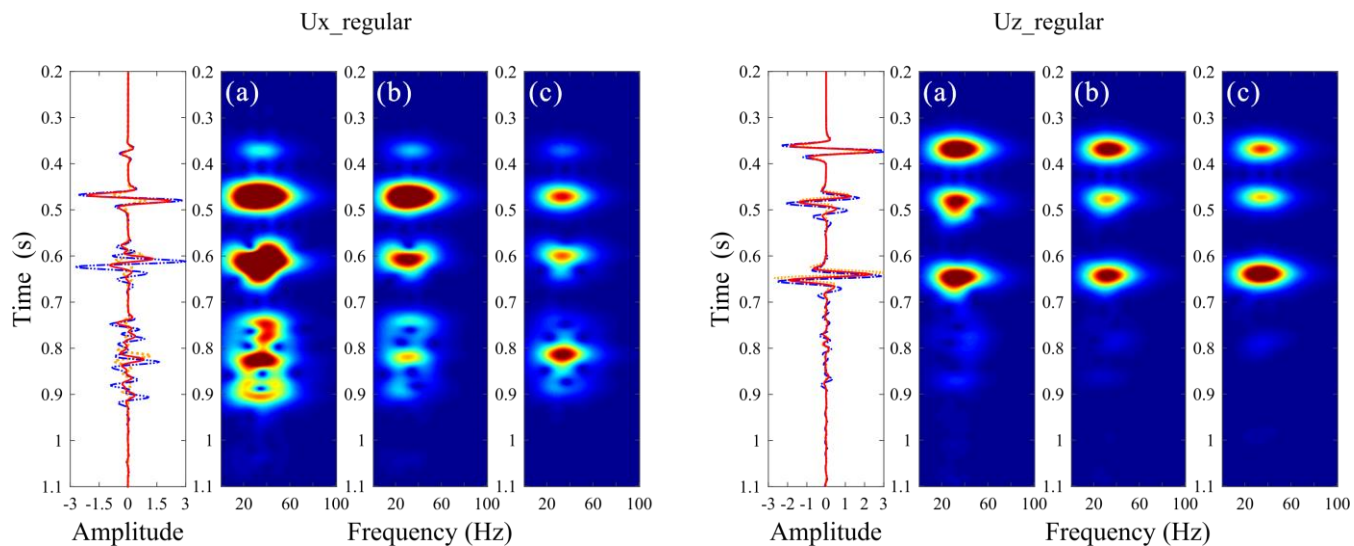


Figure 13: Time-frequency distributions of the middle trace for (b) the LVPLM, (c) the PLSM, and (d) the HVLSM cases in Figure 12.

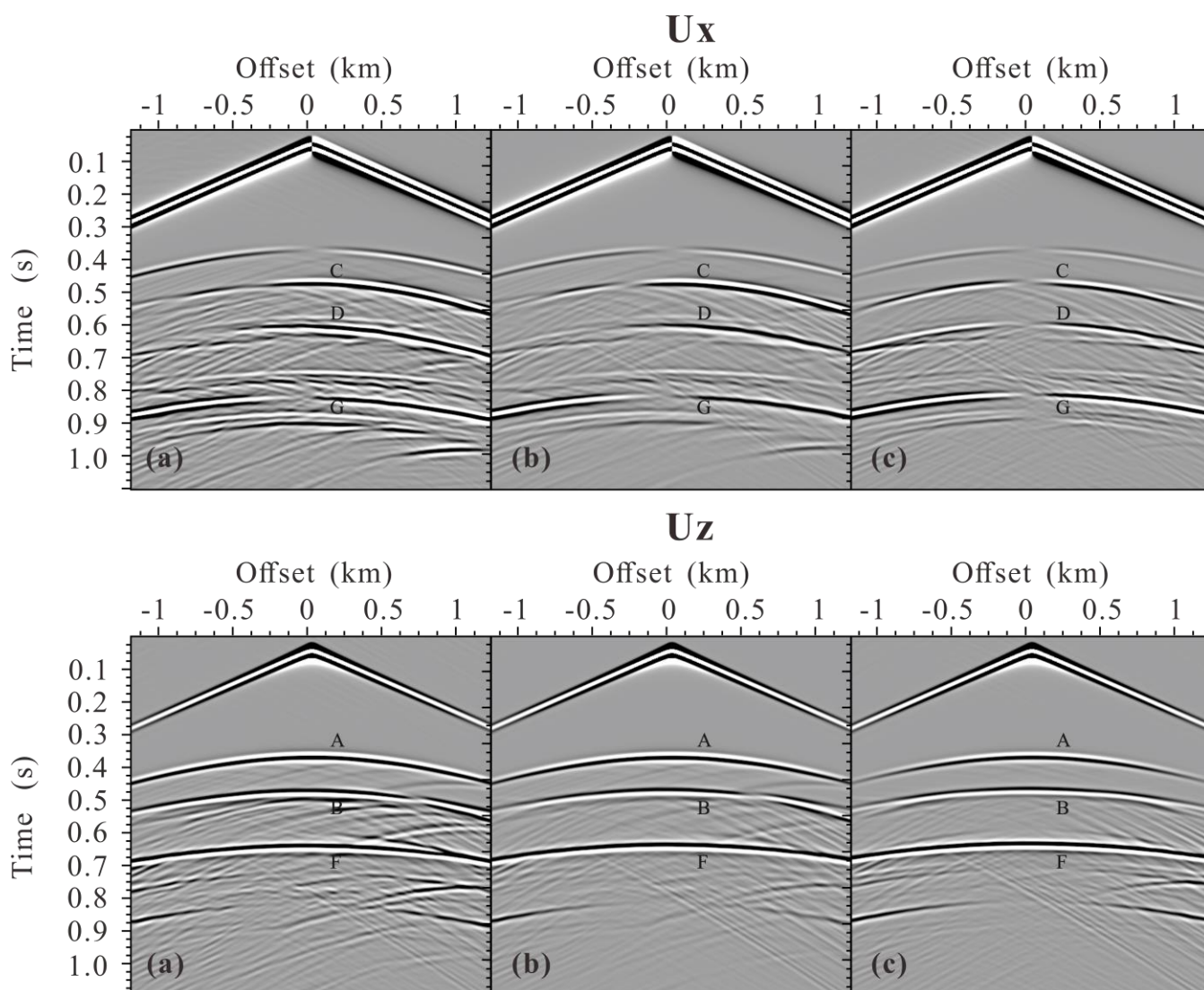


Figure 14: Seismogram components U_x and U_z of the fractured reservoir model with a set of randomly distributed aligned inclined fractures calculated using (a) the LVLSM, (b) the VLSM, (c) the HVLSM. A, B are scattered P -wave from top and bottom, respectively, C and D are scattered converted shear S -wave from top and bottom, respectively, F and G are reflected P -wave and shear converted S -wave, respectively.

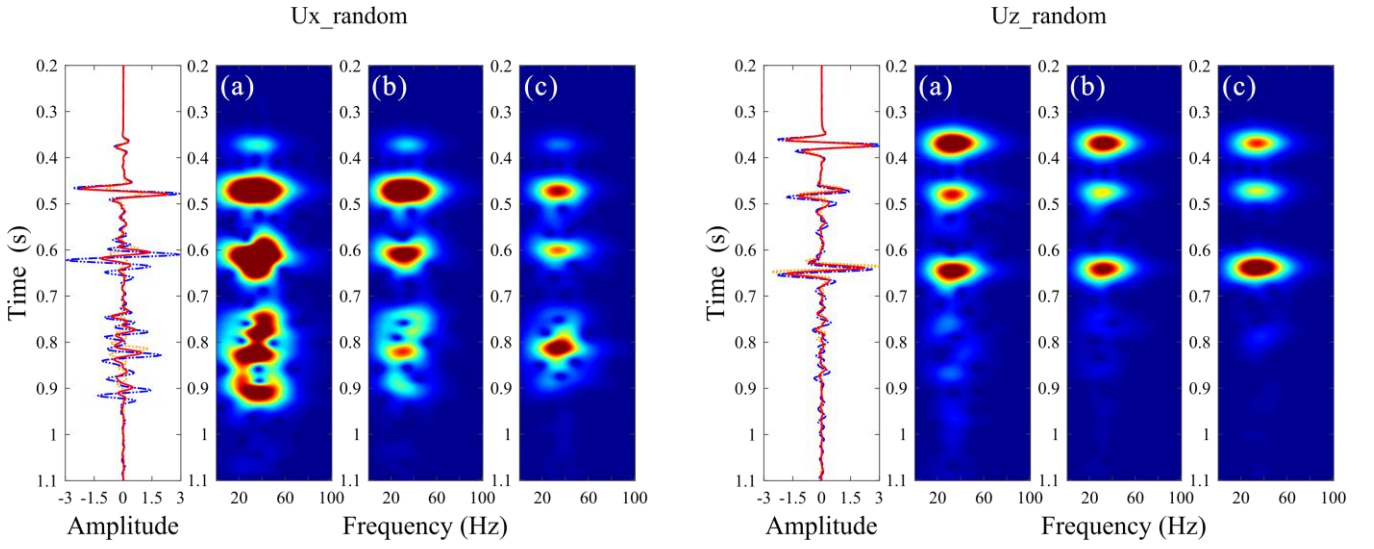


Figure 15: Time-frequency distributions of the middle trace for (b) the LVPLM, (c) the PLSM, and (d) the HVLSM cases in Figure 14.

To validate the effectiveness of our proposed modeling scheme in a more practical underground fractured reservoir, we replace a set of aligned horizontal fractures in the original model with a set of aligned inclined fractures, as illustrated in Figure 11. Figure 12 and presents the seismograms of fractured reservoir model with a set of regular distributed aligned inclined fractures and Figure 13 shows the time-frequency distributions of the middle trace for three modeling schemes. Figure 14 and Figure 15 present the seismograms of fractured reservoir model with a set of random distributed aligned inclined fractures and the time-frequency distributions of the middle trace for three modeling schemes, respectively. All results of PLSM-based modeling capture the influence of FPD effects on the amplitude and phase of scattered waves, validating the effectiveness of our proposed modeling scheme. Figure 12 and Figure 14 also show the different scattering characteristics of the randomly and regularly distributed incline fractures: many coda waves are generated by the randomly distributed fractures due to a stronger heterogeneity.

4.3 Modified Marmousi model

We test the proposed VLSM-based modeling scheme on a more complex modified Marmousi model. To modify the Marmousi model, we generate a porosity model, permeability model and discrete large-scale fracture system, and transform the original P -wave velocity and density into the fluid saturated bulk and shear modulus of the background by a constant Poisson's ratio 0.5, and finally obtain the grain bulk modulus, the frame bulk and shear modulus of the background through Gassmann equation and empirical formula ($K_m = (1 - \phi)^{\frac{3}{(1-\phi)}} K_s$). The input physical properties and elastic modulus models of the modified Marmousi model are present in Figure 11. The fluid density, bulk modulus and viscosity are the same as in Table 1. The model size is 4250m×1750m with grid interval 5m and a 100m thick PML boundary. The source is located at the surface (2125m, 0m). A Ricker wavelet with a central frequency of 25Hz is used as the temporal source excitation.

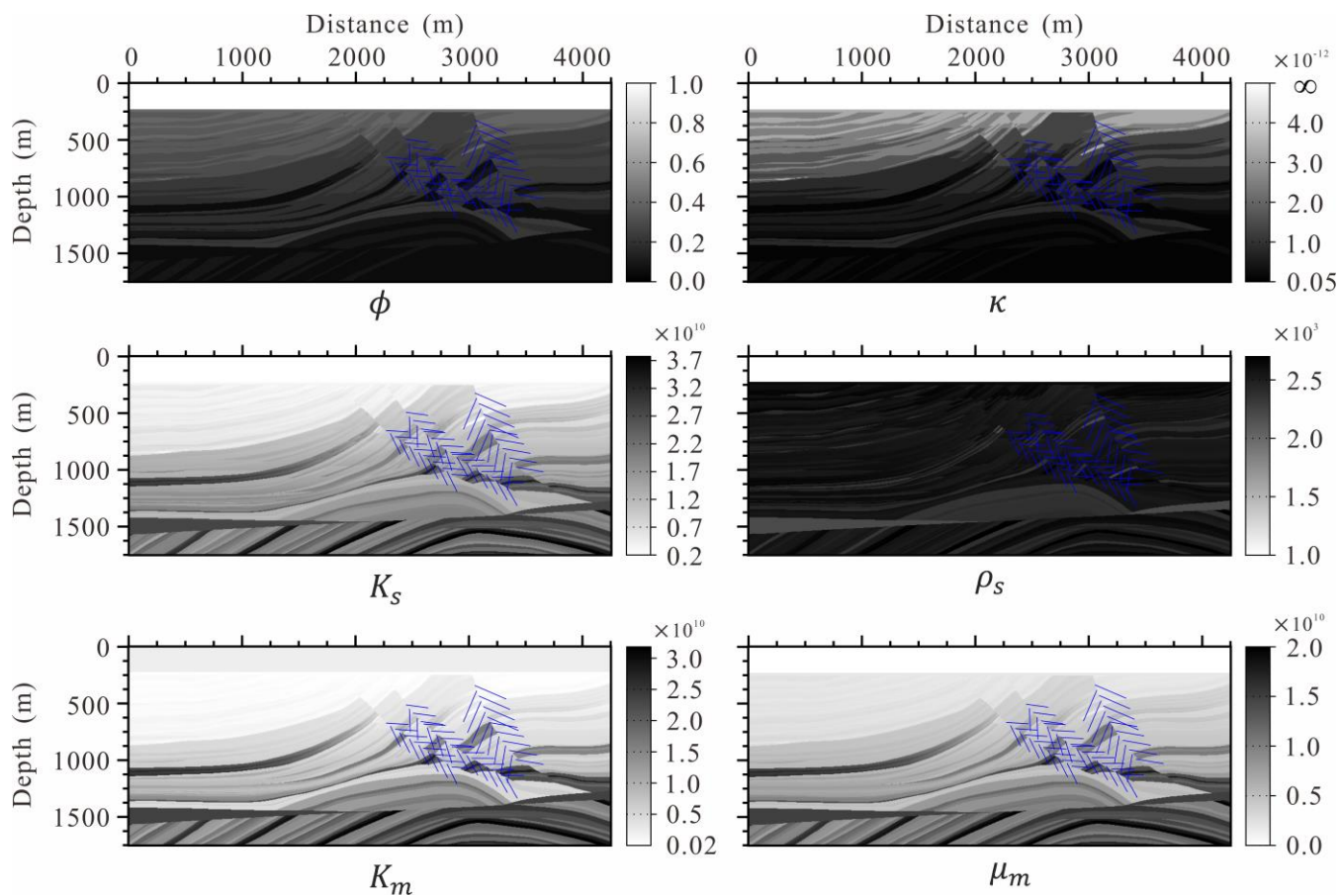


Figure 16: The physical properties and elastic modulus models of the modified Marmousi model.

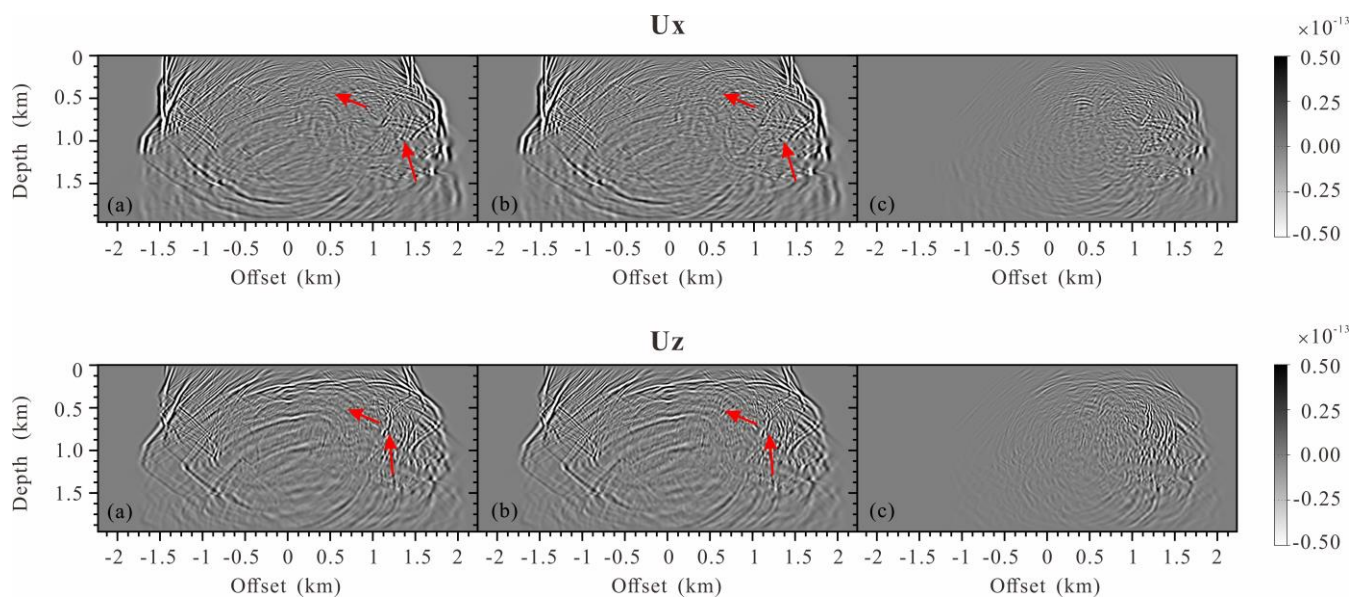


Figure 17: Snapshots of the wavefields components U_x and U_z at 1000ms: (a) the original Marmousi model without fractures, (b) the modified Marmousi model with fractures and (c) the differences.

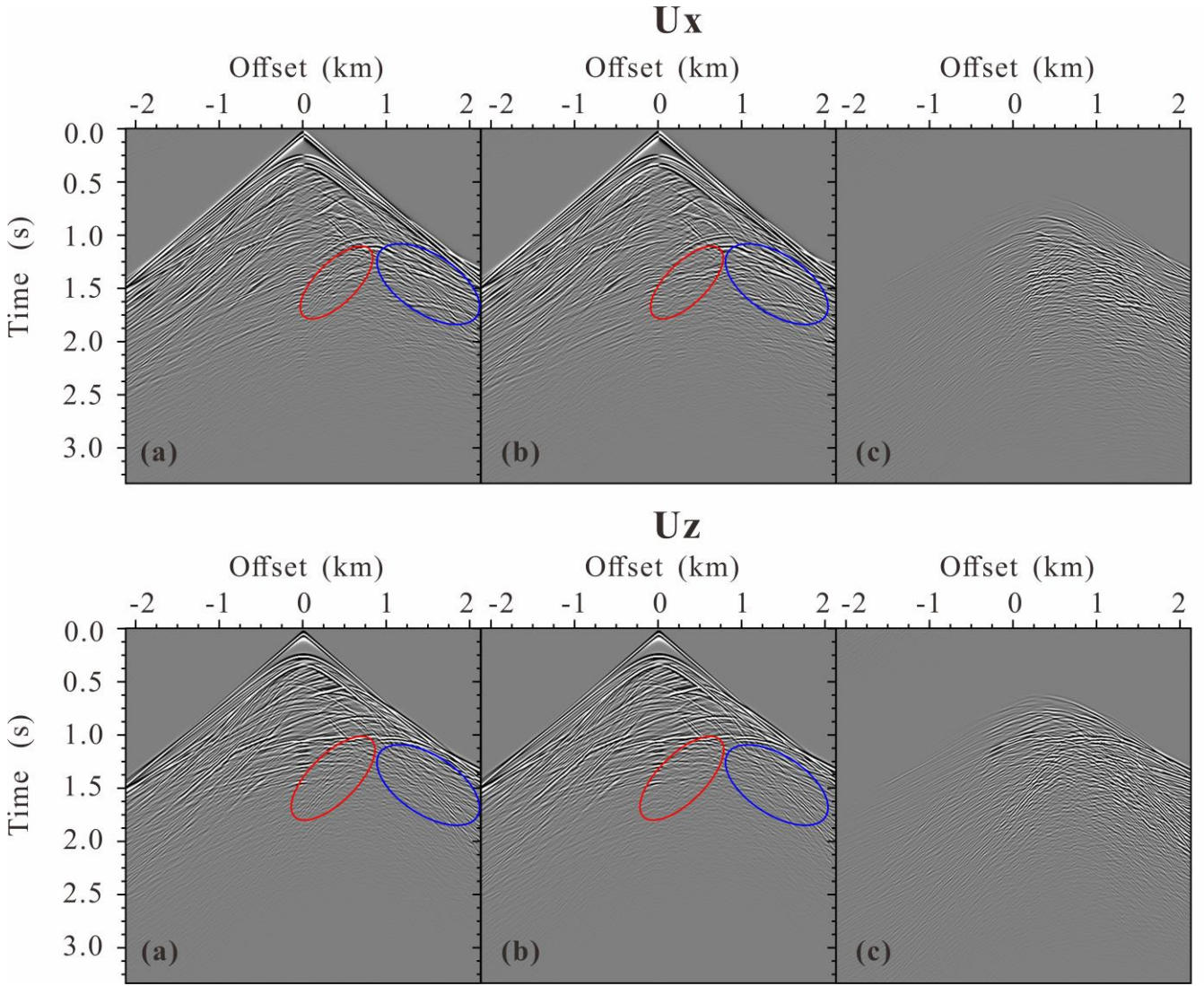


Figure 18: Seismogram components U_x and U_z : (a) the modified Marmousi model with fractures, (b) the original Marmousi model without fractures and (c) the differences.

Figures 17 shows the snapshots of displacement fields at 1000ms. The figure clearly shows the scattered P- and S-waves by the discrete distributed large-scale fractures. The results with such a complex model clearly verify the numerical implementation and the code. We also calculate the seismograms of the displacement shown in Figure 18. The seismograms obtained by our proposed modeling scheme present the scattered seismic waves by the discrete fractures.

5 Conclusions

In this work, we have developed a numerical modeling scheme including FPD effects for discrete distributed large-scale fractures embedded in fluid saturated porous rock. To capture the FPD effects between the fractures and background, the fractures are represented as Barbosa's VLMS with complex-valued and frequency-dependent fracture compliances. Using Coates and Schoenberg's local effective medium theory and Barbosa's VLMS, we derive the effective anisotropic viscoelastic compliances in each spatial discretized cell by superimposing the compliances of the background and the fractures. The effective governing equations of each numerical cell are expressed by the derived effective compliances and discretized by

471 mixed-grid stencil FDFD. The proposed modeling scheme can be used to study the impact of mechanical and hydraulic of
 472 fracture properties on seismic scattering. The main advantage of our proposed modeling scheme over poroelastic modeling
 473 schemes is that the fractured domain can be modeled using a viscoelastic solid, while the rest of the domain can be modeled
 474 using an elastic solid.

475 The scattered P -wave of a fluid saturated horizontal fracture calculated by VLSM-based modeling is strongly affected by the
 476 FPD effects, while the scattered S -wave is less sensitive, which is consistent the result of PLSM-based modeling. However,
 477 the LVLSM-based modeling overestimates the scattered P -wave and the HVLSM-based modeling underestimates the scattered
 478 P -wave. The numerical results valid that the proposed VLSM-based modeling can include the FPD effects and thus accurately
 479 estimate the scattered wave of the horizontal fracture. The results of the fractured reservoir models show that the amplitudes
 480 of the scattered waves from the top of the fractured reservoir are affected by the fluid stiffening effects due to the FPD effects.
 481 The scattered waves from the bottom of the fractured reservoir are also attenuated and dispersed by the FPD effects in addition
 482 to the fluid stiffening effects and the reflected waves can retain the relevant attenuation and dispersion information. Randomly
 483 distributed fractures can also result in a different scattering characteristic than regularly distributed fractures, i.e. a large number
 484 of coda waves are generated due to increased inhomogeneity. The results of the modified Marmousi model clearly show the
 485 scattered waves by the discrete distributed large-scale fractures and verify the proposed numerical modeling scheme. The
 486 proposed numerical modeling scheme is expected not only to improve the estimations of seismic wave scattering from discrete
 487 distributed large-scale fractures but can also to improve migration quality and the estimation of fracture mechanical
 488 characteristics in inversion.

489 **Appendix A: The coefficients related to spatial derivative operators**

490 We define coefficient vectors \mathbf{T}_k ($k = 1, 2, 3, 4$) and the derivative operate vector $\mathbf{D}(c)$ as

$$491 \quad \mathbf{T}_1 = \frac{1}{\xi_x \xi_x} [1 \ 0 \ 0 \ 0], \quad \mathbf{T}_2 = \frac{1}{\xi_x \xi_z} [0 \ 1 \ 0 \ 0], \quad \mathbf{T}_3 = \frac{1}{\xi_x \xi_z} [0 \ 0 \ 1 \ 0], \quad \mathbf{T}_4 = \frac{1}{\xi_z \xi_z} [0 \ 0 \ 0 \ 1], \quad (\text{A-1})$$

$$492 \quad \mathbf{D}(c) = [\partial_x (c \partial_x) \ \partial_x (c \partial_z) \ \partial_z (c \partial_x) \ \partial_z (c \partial_z)], \quad (\text{A-2})$$

493 where ξ_x and ξ_z are the PML damping function, c represents effective stiffness. Then, the expression of A_c, B_c, C_c, D_c are
 494 written in matrix form:

$$495 \quad \begin{bmatrix} A_c \\ B_c \\ C_c \\ D_c \end{bmatrix} = \begin{bmatrix} \mathbf{D}(c_{11}) & \mathbf{D}(c_{15}) & \mathbf{D}(c_{15}) & \mathbf{D}(c_{55}) \\ \mathbf{D}(c_{15}) & \mathbf{D}(c_{55}) & \mathbf{D}(c_{13}) & \mathbf{D}(c_{35}) \\ \mathbf{D}(c_{15}) & \mathbf{D}(c_{13}) & \mathbf{D}(c_{55}) & \mathbf{D}(c_{35}) \\ \mathbf{D}(c_{55}) & \mathbf{D}(c_{35}) & \mathbf{D}(c_{35}) & \mathbf{D}(c_{33}) \end{bmatrix} \begin{bmatrix} \mathbf{T}_1 \\ \mathbf{T}_2 \\ \mathbf{T}_3 \\ \mathbf{T}_4 \end{bmatrix}. \quad (\text{A-3})$$

496 We formulate A_r, B_r, C_r, D_r in a similar way by defining the coefficient vectors \mathbf{T}'_k ($k = 1, 2, 3, 4$) and $\mathbf{D}'(c)$ as

$$\mathbf{T}'_1 = \frac{1}{2\xi_x\xi_x}[1 \ 1 \ 1], \mathbf{T}'_2 = \frac{1}{2\xi_x\xi_z}[-1 \ 1 \ -1 \ 1], \mathbf{T}'_3 = \frac{1}{2\xi_x\xi_z}[-1 \ -1 \ 1 \ 1], \mathbf{T}'_4 = \frac{1}{2\xi_z\xi_z}[1 \ -1 \ -1 \ 1], \quad (\text{A-4})$$

$$\mathbf{D}'(c) = [\partial_{x'}(c\partial_{x'}) \ \partial_{x'}(c\partial_{z'}) \ \partial_{z'}(c\partial_{x'}) \ \partial_{z'}(c\partial_{z'})], \quad (\text{A-5})$$

The expression of A_r, B_r, C_r, D_r are written as

$$\begin{bmatrix} A_r \\ B_r \\ C_r \\ D_r \end{bmatrix} = \begin{bmatrix} \mathbf{D}'(c_{11}) & \mathbf{D}'(c_{15}) & \mathbf{D}'(c_{15}) & \mathbf{D}'(c_{55}) \\ \mathbf{D}'(c_{15}) & \mathbf{D}'(c_{55}) & \mathbf{D}'(c_{13}) & \mathbf{D}'(c_{35}) \\ \mathbf{D}'(c_{15}) & \mathbf{D}'(c_{13}) & \mathbf{D}'(c_{55}) & \mathbf{D}'(c_{35}) \\ \mathbf{D}'(c_{55}) & \mathbf{D}'(c_{35}) & \mathbf{D}'(c_{35}) & \mathbf{D}'(c_{33}) \end{bmatrix} \begin{bmatrix} \mathbf{T}'_1 \\ \mathbf{T}'_2 \\ \mathbf{T}'_3 \\ \mathbf{T}'_4 \end{bmatrix}. \quad (\text{A-6})$$

Appendix B: Parsimonious staggered-grid stencil

The nine coefficients of the CS stencil for the submatrix \mathbf{A}_c of Eq. (36):

$$A_{c \ i+1,j} = \frac{c_{11 \ i+0.5,j}}{\Delta^2 \xi_x \xi_{x \ i+0.5}}, A_{c \ i-1,j} = \frac{c_{11 \ i-0.5,j}}{\Delta^2 \xi_x \xi_{x \ i-0.5}}, A_{c \ i,j+1} = \frac{c_{55 \ i,j+0.5}}{\Delta^2 \xi_z \xi_{z \ j+0.5}}, A_{c \ i,j-1} = \frac{c_{55 \ i,j-0.5}}{\Delta^2 \xi_z \xi_{z \ j-0.5}},$$

$$A_{c \ i,j} = -\frac{c_{11 \ i+0.5,j}}{\Delta^2 \xi_x \xi_{x \ i+0.5}} - \frac{c_{11 \ i-0.5,j}}{\Delta^2 \xi_x \xi_{x \ i-0.5}} - \frac{c_{55 \ i,j+0.5}}{\Delta^2 \xi_z \xi_{z \ j+0.5}} - \frac{c_{55 \ i,j-0.5}}{\Delta^2 \xi_z \xi_{z \ j-0.5}}, A_{c \ i+1,j+1} = \frac{c_{15 \ i+1,j} + c_{15 \ i,j+1}}{4\Delta^2 \xi_x \xi_{x \ i} \xi_{z \ j}},$$

$$A_{c \ i+1,j-1} = -\frac{c_{15 \ i+1,j} + c_{15 \ i,j-1}}{4\Delta^2 \xi_x \xi_{x \ i} \xi_{z \ j}}, A_{c \ i-1,j+1} = -\frac{c_{15 \ i-1,j} + c_{15 \ i,j+1}}{4\Delta^2 \xi_x \xi_{x \ i} \xi_{z \ j}}, A_{c \ i-1,j-1} = \frac{c_{15 \ i-1,j} + c_{15 \ i,j-1}}{4\Delta^2 \xi_x \xi_{x \ i} \xi_{z \ j}}. \quad (\text{B-1})$$

The nine coefficients of the RS stencil for the submatrix \mathbf{A}_r of Eq. (36):

$$A_{r \ i+1,j} = \frac{c_{11 \ i+0.5,j-0.5} - c_{55 \ i+0.5,j-0.5}}{4\Delta^2 \xi_x \xi_{x \ i} \xi_{z \ j-0.5}} + \frac{c_{11 \ i+0.5,j+0.5} - c_{55 \ i+0.5,j+0.5}}{4\Delta^2 \xi_x \xi_{x \ i} \xi_{z \ j+0.5}}, A_{r \ i-1,j} = \frac{c_{11 \ i-0.5,j+0.5} - c_{55 \ i-0.5,j+0.5}}{4\Delta^2 \xi_x \xi_{x \ i} \xi_{z \ j+0.5}} + \frac{c_{11 \ i-0.5,j-0.5} - c_{55 \ i-0.5,j-0.5}}{4\Delta^2 \xi_x \xi_{x \ i} \xi_{z \ j-0.5}},$$

$$A_{r \ i,j+1} = \frac{c_{55 \ i-0.5,j+0.5} - c_{11 \ i-0.5,j+0.5}}{4\Delta^2 \xi_x \xi_{x \ i} \xi_{z \ j+0.5}} + \frac{c_{55 \ i+0.5,j+0.5} - c_{11 \ i+0.5,j+0.5}}{4\Delta^2 \xi_x \xi_{x \ i} \xi_{z \ j+0.5}}, A_{r \ i,j-1} = \frac{c_{55 \ i+0.5,j-0.5} - c_{11 \ i+0.5,j-0.5}}{4\Delta^2 \xi_x \xi_{x \ i} \xi_{z \ j-0.5}} + \frac{c_{55 \ i-0.5,j-0.5} - c_{11 \ i-0.5,j-0.5}}{4\Delta^2 \xi_x \xi_{x \ i} \xi_{z \ j-0.5}},$$

$$A_{r \ i,j} = -\frac{c_{11 \ i+0.5,j-0.5} - 2c_{15 \ i+0.5,j-0.5} + c_{55 \ i+0.5,j-0.5}}{4\Delta^2 \xi_x \xi_{x \ i} \xi_{z \ j-0.5}} - \frac{c_{11 \ i-0.5,j+0.5} - 2c_{15 \ i-0.5,j+0.5} + c_{55 \ i-0.5,j+0.5}}{4\Delta^2 \xi_x \xi_{x \ i} \xi_{z \ j+0.5}} \\ - \frac{c_{11 \ i+0.5,j+0.5} + 2c_{15 \ i+0.5,j+0.5} + c_{55 \ i+0.5,j+0.5}}{4\Delta^2 \xi_x \xi_{x \ i} \xi_{z \ j+0.5}} - \frac{c_{11 \ i-0.5,j-0.5} + 2c_{15 \ i-0.5,j-0.5} + c_{55 \ i-0.5,j-0.5}}{4\Delta^2 \xi_x \xi_{x \ i} \xi_{z \ j-0.5}}$$

$$A_{r \ i+1,j+1} = \frac{c_{11 \ i+0.5,j+0.5} + 2c_{15 \ i+0.5,j+0.5} + c_{55 \ i+0.5,j+0.5}}{4\Delta^2 \xi_x \xi_{x \ i} \xi_{z \ j+0.5}}, A_{r \ i+1,j-1} = \frac{c_{11 \ i+0.5,j-0.5} - 2c_{15 \ i+0.5,j-0.5} + c_{55 \ i+0.5,j-0.5}}{4\Delta^2 \xi_x \xi_{x \ i} \xi_{z \ j-0.5}},$$

$$A_{r \ i-1,j+1} = \frac{c_{11 \ i-0.5,j+0.5} - 2c_{15 \ i-0.5,j+0.5} + c_{55 \ i-0.5,j+0.5}}{4\Delta^2 \xi_x \xi_{x \ i} \xi_{z \ j+0.5}}, A_{r \ i-1,j-1} = \frac{c_{11 \ i-0.5,j-0.5} + 2c_{15 \ i-0.5,j-0.5} + c_{55 \ i-0.5,j-0.5}}{4\Delta^2 \xi_x \xi_{x \ i} \xi_{z \ j-0.5}}. \quad (\text{B-2})$$

The coefficients of the submatrices $\mathbf{B}_c, \mathbf{C}_c, \mathbf{D}_c$ and $\mathbf{B}_r, \mathbf{C}_r, \mathbf{D}_r$ can be inferred easily from those of submatrix \mathbf{A}_c and \mathbf{A}_r , respectively.

514 **Acknowledgments**

515 This research was financially supported by the National Natural Foundation of China (grant nos. 41874143 and 41574130)
516 and the Key Program of Natural Science Foundation of Sichuan Province (No. 23NSFC0139).

517 **References**

- 518 Barbosa, N. D., Rubino J. G., Caspari E., and Holliger K.: Extension of the classical linear slipmodel for fluid-saturated
519 fractures: Accounting for fluid pressure diffusion effects, *J. Geophys. Res.*, 122, 1302-1323, doi:10.1002/2016JB013636,
520 2016a.
- 521 Barbosa, N. D., Rubino J. G., Caspari E., Milani M., and Holliger K.: Fluid pressure diffusion effects on the seismic reflectivity
522 of a single fracture, *J. Acoust. Soc. Am.*, 140, 2554-2570, doi:10.1121/1.4964339, 2016b.
- 523 Biot, M. A.: Theory of elastic waves in a fluid-saturated porous solid. I. Low frequency range, *J. Acoust. Soc. Am.*, 28, 168-
524 178, doi:10.1121/1.1908239, 1956a.
- 525 Biot, M. A.: Theory of elastic waves in a fluid-saturated porous solid. II. High frequency range, *J. Acoust. Soc. Am.*, 28, 179-
526 191, doi:10.1121/1.1908241, 1956b.
- 527 Brajanovski, M., Gurevich, B., and Schoenberg, M.: A model for *P*-wave attenuation and dispersion in a porous medium
528 permeated by aligned fractures, *Geophys. J. Int.*, 163, 372-384, doi:10.1111/j.1365-246X.2005.02722.x, 2005.
- 529 Brajanovski, M., Müller T. M., and Gurevich B.: Characteristic frequencies of seismic attenuation due to wave-induced fluid
530 flow in fractured porous media, *Geophys. J. Int.*, 166, 574-578, doi:10.1111/j.1365-246X.2006.03068.x, 2006.
- 531 Chapman, M.: Frequency dependent anisotropy due to mesoscale fractures in the presence of equant porosity, *Geophys.*
532 *Prospect.*, 51, 369-379, doi:10.1046/j.1365-2478.2003.00384.x, 2003.
- 533 Coates, R. T. and Schoenberg, M.: Finite-difference modeling of faults and fractures, *Geophysics*, 60, 1514-1526,
534 doi:10.1190/1.1443884, 1995.
- 535 Cui, X. Q., Lines, L. R., and Krebs, E. S.: Seismic modelling for geological fractures, *Geophys. Prospect.*, 2018,157-168,
536 doi:10.1111/1365-2478.12536, 2018.
- 537 Dutta, N. C. and Odé, H.: Attenuation and dispersion of compressional waves in fluid-filled porous rocks with partial gas
538 saturation (White Model)-Part I: Biot theory, *Geophysics*, 44, 1777-1788, doi:10.1190/1.1440938, 1979a.
- 539 Dutta, N. C. and Odé, H.: Attenuation and dispersion of compressional waves in fluid-filled porous rocks with partial gas
540 saturation (White Model)-Part II: Results, *Geophysics*, 44, 1806-1812, doi:10.1190/1.1440939, 1979b.
- 541 Gale, J. F. W., Laubach S. E., Olson J. E., Eichhubl P., and Fall A.: Natural fractures in shale: A review and new observations:
542 AAPG Bulletin, 98, 2165-2216, doi:10.1306/08121413151, 2014.
- 543 Galvin, R. J. and Gurevich, B.: Frequency-dependent anisotropy of porous rocks with aligned fractures, *Geophys. Prospect.*,

544 63, 141-150, doi:10.1071/ASEG2003ab016, 2015.

545 Gassmann, F.: Elastic waves through a packing of spheres, *Geophysics*, 16, 673-685, doi:10.1190/1.1437718, 1951.

546 Gavagnin, C., Sanavia, L., and Lorenzis, L. D.: Stabilized mixed formulation for phase-field computation of deviatoric fracture
547 in elastic and poroelastic materials, *Comput Mech*, 65, 1447-1465, doi:10.1007/s00466-020-01829-x, 2020.

548 Gelinsky, S. and Shapiro, S. A.: Dynamic-equivalent medium approach for thinly layered saturated sediments, *Geophys. J. Int.*,
549 128, F1-F4, doi:10.1111/j.1365-246X.1997.tb04086.x, 1997.

550 Guo J. X., Rubino J. G., Barbosa, N. D., Glubokovskikh, S. G., and Gurevich, B.: Seismic dispersion and attenuation in
551 saturated porous rocks with aligned fractures of finite thickness: Theory and numerical simulations—Part I: *P*-wave
552 perpendicular to the fracture plane, *Geophysics*, 83, 49-62, doi:10.1190/geo2017-0065.1, 2017a.

553 Guo J. X., Rubino J. G., Barbosa, N. D., Glubokovskikh, S. G., and Gurevich, B.: Seismic dispersion and attenuation in
554 saturated porous rocks with aligned fractures of finite thickness: Theory and numerical simulations—Part II: Frequency-
555 dependent anisotropy, *Geophysics*, 83, 63-71, doi:10.1190/geo2017-0066.1, 2017b.

556 Gurevich, B., Zyrianov, V. B., and Lopatnikov, S. L.: Seismic attenuation in finely layered porous rocks: Effects of fluid flow
557 and scattering, *Geophysics*, 62(1), 319-324, doi:10.1190/1.1444133, 1997.

558 Gurevich, B.: Elastic properties of saturated porous rocks with aligned fractures, *J. Geophys. Res.*, 54, 203-218,
559 doi:10.1016/j.jappgeo.2002.11.002, 2003.

560 Hustedt, B., Operto S., and Virieux J.: Mixed-grid and staggered-grid finite difference methods for frequency domain acoustic
561 wave modelling, *Geophys J Int*, 157, 1269-1296, doi:10.1111/j.1365-246X.2004.02289.x, 2004.

562 Johnson, D. L.: Theory of frequency dependent acoustics in patchy-saturated porous media, *J. Acoust. Soc. Am.*, 110(2), 682-
563 694, doi:10.1121/1.1381021, 2001.

564 Jo, C.H., Shin, C.S., and Suh, J.H.: An optimal 9-point, finite-difference, frequency-space, 2-D scalar wave extrapolator,
565 *Geophysics*, 61, 529-537, doi:10.1190/1.1443979, 1996.

566 Khokhlov, N., Favorskaya, A., Stetsyuk, V., Mitskovets, I.: Grid-characteristic method using Chimera meshes for simulation
567 of elastic waves scattering on geological fractured zones, *J. Comput. Phys.*, 446, 110637, doi:10.1016/j.jcp.2021.110637,
568 2021.

569 Krzikalla, F. and Müller T. M.: Anisotropic P-SV-wave dispersion and attenuation due to inter-layer flow in thinly layered
570 porous rocks, *Geophysics*, 76, WA135-WA145, doi:10.1190/1.3555077, 2011.

571 Kudarova, A. M., Karel, V. D., and Guy D.: An effective anisotropic poroelastic model for elastic wave propagation in finely
572 layered media, *Geophysics*, 81, 175-188, doi:10.1190/geo2015-0362.1, 2016.

573 Liu E. R., Hudson J. A., and Pointer T.: Equivalent medium representation of fractured rock, *J. Geophys. Res.*, 105, 2981-3000,
574 doi:10.1029/1999JB900306, 2000.

575 Liu, X., Greenhalgh, S., Zhou, B., and Greenhalgh, M.: Frequency-domain seismic wave modelling in heterogeneous porous

media using the mixed-grid finite-difference method, *Geophys J Int.*, 216, 34-54, doi:10.1093/gji/ggy410, 2018.

Müller, T. M., Stewart J. T., and Wenzlau, F.: Velocity-saturation relation for partially saturated rocks with fractal pore fluid distribution, *Geophys. Res. Lett.*, 35, L09306, doi:10.1029/2007GL033074, 2008.

Nakagawa, S. and Schoenberg M. A.: Poroelastic modeling of seismic boundary conditions across a fracture, *J. Acoust. Soc. Am.*, 122, 831-847, doi:10.1121/1.2747206, 2007.

Norris, A. N.: Low-frequency dispersion and attenuation in partially saturated rocks, *J. Acoust. Soc. Am.*, 94, 359-370, doi:10.1121/1.407101, 1993.

Oelke, A., Alexandrov, D., Abakumov, I., Glubokovskikh, S., Shigapov, R., Krüger, O. S., Kashtan, B., Troyan, V., and Shapiro, S. A.: Seismic reflectivity of hydraulic fractures approximated by thin fluid layers, *Geophysics*, 78, 79-87, doi:10.1190/geo2012-0269.1, 2013

Operto, S., Virieux, J., Ribodetti, A., and Anderson J. E.: Finite-difference frequency-domain modeling of viscoacoustic wave propagation in 2D tilted transversely isotropic (TTI) media, *Geophysics*, 74, 75-95, doi:10.1190/1.3157243, 2009.

Rubino, J. G., Müller T. M., Guarracino L., Milani M., and Holliger K.: Seismoacoustic signatures of fracture connectivity, *J. Geophys. Res. Solid Earth.*, 119, 2252-2271, doi:10.1002/2013JB010567, 2014.

Rubino, J. G., Castromán G. A., Müller T. M., Monachesi L. B., Zyserman F. I., and Holliger K.: Including poroelastic effects in the linear slip theory, *Geophysics*, 80, A51-A56, doi:10.1190/geo2014-0409.1, 2015.

Sayers, C. M. and Kachanov M.: Microcrack-induced elastic wave anisotropy of brittle rocks, *J. Geophys. Res.*, 100, 4149-4156, doi:10.1029/94JB03134, 1995.

Schoenberg, M. A.: Elastic wave behavior across linear slip interfaces, *J. Acoust. Soc. Am.*, 68, 1516-1521, doi:10.1121/1.385077, 1980.

White, J. E., Mikhahaylova, N. G., and Lyakhovitsky, F. M.: Low-frequency seismic waves in fluid-saturated layered rocks, *Izv., Acad. Sci., USSR, Phys. Solid Earth.*, 11, 654-659, doi:10.1121/1.1995164, 1975.

Zhang, J. F.: Elastic wave modeling in fractured media with an explicit approach, *Geophysics*, 70, 75-85, doi:10.1190/1.2073886, 2005.